A three-dimensional process-based morphodynamic model on orthogonal unstructured grids for coastal applications

Reyns, Johan; Jagers, Bert; Ranasinghe, Roshanka; Kernkamp, Herman; Roelvink, Dano

DOI
10.1016/j.coastaleng.2025.104915

Publication date
2025

Document Version
Final published version

Published in
Coastal Engineering

Citation (APA)
Reyns, J., Jagers, B., Ranasinghe, R., Kernkamp, H., & Roelvink, D. (2025). A three-dimensional process-based morphodynamic model on orthogonal unstructured grids for coastal applications. *Coastal Engineering*, *204*, Article 104915. https://doi.org/10.1016/j.coastaleng.2025.104915

Coastal Engineering 204 (2026) 104915

Contents lists available at ScienceDirect

Coastal Engineering

journal homepage: www.elsevier.com/locate/coastaleng

A three-dimensional process-based morphodynamic model on orthogonal unstructured grids for coastal applications

Johan Reyns [a,b,c,*], Bert Jagers [b], Roshanka Ranasinghe [a,b,d], Herman Kernkamp [b], Dano Roelvink [a,b,c]

[a] IHE Delft Institute for Water Education, PO Box 3015, 2601 DA, Delft, The Netherlands
[b] Deltares, Boussinesqweg 1, 2629 HV, Delft, The Netherlands
[c] Faculty Civil Engineering and Geosciences, Delft University of Technology, Stevinweg 1, 2628 CN, Delft, The Netherlands
[d] Department of Water Engineering and Management, University of Twente, PO Box 217, 7500 AE, Enschede, The Netherlands

ARTICLE INFO

Keywords:
Process-based modelling
Morphodynamics
Wave–current interaction
Unstructured meshes

ABSTRACT

This study presents a 3D process-based morphodynamic model that uses orthogonal unstructured grids. It is designed for coastal applications involving complex bathymetry and varying spatial scales. The model extends the Delft3D-FM framework by incorporating full 3D representation of wave, wind, and density-driven effects in the short-wave-averaged, non-linear shallow water equations. The framework includes expressions for wave and roller effects on flow forcing, turbulence, and bed shear stress, and integrates sediment transport and morphodynamic feedback. Multi-fraction sediment transport is supported, and the model tracks stratigraphy through a layered bed composition framework. Features such as infragravity wave dynamics, sediment mass slumping, swash zone slope nudging and morphological acceleration techniques are incorporated to better capture long-term morphological trends as well as storm erosion. The framework supports in-memory model coupling and is fully parallelized, enabling efficient, large-scale simulations. Model verifications presented here include analytical benchmarks and comparisons with laboratory and field observations, demonstrating reliable reproduction of wave–current interaction, sediment transport rates, and bed level changes. The model has the potential to bridge the gap between high-resolution event-scale modelling and long-term morphodynamic prediction, offering a flexible framework to study coastal sedimentary dynamics.

1. Introduction

The morphology of coastal areas is shaped by sediment transport patterns resulting from atmospheric and oceanographic forcing, and it is constrained by the region's underlying geological setting. Over time, coasts have become hotspots for socio-economic development, and this trend is expected to continue in the future (Dodman et al., 2022). As a result, the anthropogenic footprint on the morphodynamics of coastal environments is large, and this interplay is projected to grow further in many places worldwide (Nawarat et al., 2024). Future changes in storminess (Priestley and Catto, 2022), wave climate (Lobeto et al., 2022), sea level rise (Fox-Kemper et al., 2021) and riverine sediment supply (Nienhuis and van de Wal, 2021; Dethier et al., 2022) are all expected to impact coastal morphology in various ways and at different degrees, which poses significant challenges for sustainable coastal zone management.

To safeguard the sustainability of the ecological, societal and economic functioning of the low elevation coastal zone, integrated coastal zone management practitioners need quantitative information about the hydro-sedimentary system on the relevant time– and spatial scales, to inform the decision making process (Cuddington et al., 2013; Wu and Wan, 2024). This information need has motivated a substantial body of research on data-driven and numerical coastal modelling over the last decades, resulting in several approaches that have reached different levels of maturity (Hunt et al., 2023). Among these modelling approaches, process-based morphodynamic models remain one of the most popular choices, owing to being the most physically sound method, and to the direct relevance of the spatio-temporal scales they typically resolve.

Traditionally cited drawbacks of this class of numerical models, such as a high computational demand, and decreased reliability over longer timescales (Reeve et al., 2016), have been addressed by a number of recent developments. The implementation of parallelization techniques such as shared and distributed memory calculations, and GPU acceleration (Afzal et al., 2016), in combination with the improved accessibility of computational clusters and cloud computing

* Corresponding author.
E-mail address: j.reyns@un-ihe.org (J. Reyns).

https://doi.org/10.1016/j.coastaleng.2025.104915
Received 26 June 2025; Received in revised form 12 September 2025; Accepted 25 November 2025
Available online 27 November 2025

have significantly reduced the computational time associated with process-based modelling. The increase in the number and the temporal coverage of publicly available global and regional datasets of topo-bathymetry (Weatherall et al., 2015; Guth et al., 2024), land cover (Xu et al., 2024), and hydro-meteorological variables (Hersbach et al., 2020; Egbert and Erofeeva, 2002; Chassignet et al., 2007) now facilitate the implementation of process-based models in many regions in the world. The recent push to make many of the frequently used process-based modelling frameworks available as open source code has aided in their wide adoption within both the research and engineering consulting communities. Input reduction techniques (Latteux, 1995; Walstra et al., 2013) and algorithmic developments such as morphological acceleration and in–memory ensemble averaging of morphodynamics (Roelvink, 2006), have extended the temporal applicability of process-based models from years to decades. The use of unstructured grids improves the efficiency of domain discretization and optimizes the explicit part of the time integration of numerical models (Reyns et al., 2023). It allows for targeted local spatial refinement where needed to improve model results in cases with complex boundaries or large spatial gradients in bathymetry, cases that typically pose challenges to model performance when using a cartesian or curvilinear grid administration (e.g., López-Ramade et al., 2023).

Coastal process-based morphodynamic models are typically used to assess morphological changes from storm events (O(days)) to interannual timescales (Hunt et al., 2023). While the physical processes that are influencing the morphological development over time are essentially the same, their importance varies according to the timescale under consideration (Sherwood et al., 2022). This distinction has led to the development of different models for different timescales. For example, the popular XBeach model (Roelvink et al., 2009), which resolves the event timescale, has become the *de facto* standard for assessing erosion hazards under the different Sallenger (2000) regimes, due to its strong focus on wave group-related hydrodynamics and storm-related morphodynamics. Other models, such as TELEMAC (Villaret et al., 2013), MIKE21 (Zyserman and Johnson, 2002) and FVCOM (Chen et al., 2006), are applied to assess the morphodynamics on timescales of weeks to years. Models that bridge this divide, and contain the necessary physics to integrate processes over a large range of spatiotemporal scales within one framework, remain scarce. One notable exception is the curvilinear COAWST model (Warner et al., 2010), which was recently extended with a module for infragravity wave dynamics and dune front slumping (Olabarrieta et al., 2023). To date, no unstructured models with a similar functionality exist. The description of such an unstructured model, and the demonstration of its key functionality by comparing model outcomes with analytical solutions, and laboratory and field observations is the aim of this paper.

The present model extends Delft3D-FM (Kernkamp et al., 2011; Martyr-Koller et al., 2017; Reyns et al., 2023) by incorporating 3D wave effects in the hydrodynamic solver, and by adding additional sediment transport and morphodynamic capabilities, building upon and combining the approaches of Lesser et al. (2004) for detailed sediment and morphology processes with the features for storm impact assessment of Roelvink et al. (2009). This unique modelling approach allows for new applications such as a large-scale, but a locally very detailed, model of the response of a complex beach/dune system to a large storm, or the 3D morphological modelling of a field of offshore breakwaters.

The outline of this paper is as follows. Section 2 describes the model formulations. Section 3 describes the numerical aspects of the implementation. Section 4 presents model verification results for hydrodynamics (Section 4.1), sediment transport (Section 4.2) and morphodynamics (Section 4.3). Finally, Section 5 contains discussion and conclusions.

2. Model formulations

The model solves the short-wave-averaged, non-linear shallow water equations, accounting for the effects of waves, wind, and density-driven flows. It extends the 3D unstructured Delft3D-FM flow model (Kernkamp et al., 2011; Martyr-Koller et al., 2017) by incorporating additional terms to represent depth-varying wave-induced forcing, bed shear stress, and turbulence. Furthermore, it includes modules for sediment transport and morphological evolution.

In this work, we apply the following definitions for the grid geometry. In the vertical, we discretize the domain in a fixed number of layers n_{lay}, using terrain-following σ coordinates. Layers are separated by layer interfaces, where the lowest interface corresponds to the bed, and the top interface to the free water surface. In the horizontal direction, each layer of the orthogonal unstructured mesh is discretized in cells, which are each bounded by a set of faces. Each cell has a base surface area S and a volume V. The horizontal positions of variables in each cell are staggered, with scalars being defined in the cell centre, and the face-normal and face-tangential velocity components and fluxes being defined at the midpoint of every cell face. The vertical velocities are defined in the midpoints of the interface separating neighbouring cells within the same column of water.

2.1. Hydrodynamics

2.1.1. Wave module

In order to incorporate wave effects on the nearshore circulation in our model, we need space and time-varying estimations of integral quantities like wave heights, periods, and directions, and of wave dissipation. In this study, we adopt two different wave models, depending on the application. The first wave model is the curvilinear version of the SWAN model (Booij et al., 1999), the second wave driver is the wave group-scale resolving wave model of Reyns et al. (2023). Here, we only give a short description of the model features, and we refer to the referenced literature for more details.

SWAN model (Booij et al., 1999). The third-generation spectral SWAN model solves the spectral wave action balance for random, directionally-spread wind-generated waves as a function of prevailing wind, currents, water depth and bathymetry (Eq. (1)).

$$\frac{\partial A}{\partial t} + \nabla \cdot \boldsymbol{c_g} A + \frac{\partial c_\theta A}{\partial \theta} + \frac{\partial c_\omega A}{\partial \omega} = S_{\text{wave}}, \tag{1}$$

where $A(t, x, y, \theta, \omega)$ is the time- and space-varying wave action as a function of both wave direction and frequency, t is time, $\boldsymbol{c_g}$ is the wave group velocity vector, c_θ is the refraction velocity, θ is the wave direction, ω is the relative wave frequency, and c_ω is a measure for the speed of frequency shift of wave action A. ∇ represents the spatial gradient operator $\boldsymbol{i}\frac{\partial}{\partial x} + \boldsymbol{j}\frac{\partial}{\partial y}$, with $\boldsymbol{i}$ and $\boldsymbol{j}$ the unit vectors in x- and y-direction, respectively. The model source and sink terms S_{wave} incorporate wind growth, non-linear wave-wave interaction by quadruplets and triads, dissipation by bed friction, whitecapping, depth-induced wave breaking, and by vegetation. The model accounts for shoaling, depth- and current-induced refraction, diffraction and reflection (Booij et al., 1999; Holthuijsen et al., 2003). The coupling in this study is performed in an online manner, where at predetermined time points flow and wave information is exchanged using communication files and interpolation. We apply the well tested and stable curvilinear grid version, which can be used in a nested configuration to reach the desired spatial resolution to resolve the wave physics of interest. Although an unstructured version of SWAN (UnSWAN; Zijlema, 2010) is available, it is less extensively validated. Moreover, UnSWAN employs triangular grids, which still necessitate interpolation when coupling with the mixed-element unstructured grids used in Delft3D-FM.

Wave group-scale model of Reyns et al. (2023). The wave model of Reyns et al. (2023) solves a reduced version of the wave action balance (Eq. (1)) in stationary or non-stationary mode, and is designed for local-scale surf zone applications. The model accounts for shoaling and refraction only, not for changes in wave period (i.e. $A(t,x,y,\theta)$). Wave action sinks are limited to dissipation by bed friction and depth-induced wave breaking, and wind growth is not supported. During non-stationary runs, wave boundary conditions are provided at the time scale of wave groups, which allows simulating the generation and propagation of infragravity waves. Additionally, the model features a coupled solver for the roller energy balance, which improves estimates of wave-driven currents in the nearshore (Nairn et al., 1990). In contrast to SWAN, the model of Reyns et al. (2023) is directly integrated in the Delft3D-FM code, and shares its spatial discretization with the flow module. During stationary runs, the wave and roller energy fields are updated at a user-defined time interval. Non-stationary runs are tightly coupled with the circulation model, and update the wave-related quantities at every time step.

2.1.2. Flow module

The circulation model is based on Kernkamp et al. (2011) and Martyr-Koller et al. (2017), with additions to account for the effect of waves. The flow module resolves the continuity and momentum equations for incompressible flow in two or three dimensions (Eqs. (3) and (4), respectively). We treat the pressure as hydrostatic, and we divide it in a barotropic and a baroclinic part, to take into account the effects of salt, temperature and sediment on the fluid density (Eq. (2)):

$$\frac{\partial p}{\partial z} = -\rho g, \qquad p = \overline{p} + p', \tag{2}$$

where p is the total pressure, $\overline{p}$ is the barotropic pressure contribution, p' is the baroclinic pressure part, z is the vertical coordinate, ρ is the mean fluid density, potentially with the influence of the presence of sediment, and g is the gravitational acceleration. Sediment effects on fluid density are taken into account as $\rho = \rho_w + \sum_{nf} c_i\,(\rho_{i,s} - \rho_w)/\rho_{i,s}$, with nf the number of fractions, i is the suspended fraction under consideration, ρ_w the water density, c_i the sediment concentration, and $\rho_{i,s}$ the density of the solid particles. The flow equations are expressed in Generalized Lagrangian Mean velocities (GLM) $\boldsymbol{u}$ (Andrews and McIntyre, 1978; Nguyen et al., 2021), defined as the sum of the Eulerian velocities $\boldsymbol{u}^E$, the velocity field observed from a fixed point at the bed, and the vertically varying Stokes drift $\boldsymbol{u}^S$ (Eq. (6)), calculated from linear wave theory. The continuity equation reads

$$\frac{\partial h}{\partial t} + \nabla \cdot (h\boldsymbol{u}) = S_{\text{flow}} \tag{3}$$

The momentum balance reads

$$\frac{\partial \boldsymbol{u}}{\partial t} + \nabla\cdot(\boldsymbol{u}\boldsymbol{u}) + \frac{\partial u_z \boldsymbol{u}}{\partial z} = -\boldsymbol{g}\cdot\nabla\eta - \frac{1}{\rho}\nabla p' + \nabla\cdot(\nu_h(\nabla\boldsymbol{u} + \nabla\boldsymbol{u}^T)) + \frac{\partial}{\partial z}(\nu_z \frac{\partial \boldsymbol{u}}{\partial z}) - f_{\text{cor}}\hat{\boldsymbol{e}}_z \times \boldsymbol{u} + \boldsymbol{F}, \tag{4}$$

and is subject to zero-flux bed and surface boundary conditions and to

$$\nu_z \frac{\partial \boldsymbol{u}}{\partial z}\bigg|_{z=\text{bed}} = \frac{1}{\rho}\boldsymbol{\tau_b}, \qquad \nu_z \frac{\partial \boldsymbol{u}}{\partial z}\bigg|_{z=\text{surface}} = f_{wd}\frac{\rho_a}{\rho}|\boldsymbol{u_w}|\boldsymbol{u_w} + \frac{\boldsymbol{F}_{\text{wave,s}}}{\rho}, \tag{5}$$

where h is the water depth, t is time, z is the vertical coordinate, $\boldsymbol{u} = \{u_x, u_y\}$ is the vector of horizontal GLM velocities, u_z is the vertical component of the velocity vector, S_{flow} is the source term for mass, including discharges, evaporation and precipitation, g is the gravitational acceleration, ρ is the mean density, ν_h is the horizontal viscosity coefficient, ν_z is the vertical viscosity coefficient, f_{cor} is the latitude dependent Coriolis parameter, $\hat{\boldsymbol{e}}_z$ is the unit vector in positive vertical direction, $\boldsymbol{F}$ are the forces due to air pressure, tidal forces and waves; $\boldsymbol{\tau_b}$ is the (potentially wave-enhanced) bed shear stress; f_{wd} is the wind friction factor; ρ_a is the air density; $\boldsymbol{u_w}$ is the wind velocity vector at 10 m above the surface; and $\boldsymbol{F}_{\text{wave,s}}$ is the wave force vector at the water surface. The Stokes drift vector $\boldsymbol{u}^S$ is calculated from Dean and Dalrymple (1991):

$$\boldsymbol{u}^S = \frac{H_{rms}^2}{8}\,\boldsymbol{k}\,\omega\frac{\cosh 2|\boldsymbol{k}|(z+h)}{\sinh^2|\boldsymbol{k}|h}, \tag{6}$$

where H_{rms} is the RMS wave height, $\boldsymbol{k}$ is the wave number vector, ω is the wave frequency, and z is the vertical coordinate. Both $\boldsymbol{k}$ and ω are derived based on the peak wave period. Near the bed, wave streaming is modelled as a time-averaged shear stress, varying over the thickness of the wave boundary layer δ (Fredsøe and Deigaard, 1992), and added to $\boldsymbol{F}$:

$$-\frac{\partial \overline{\tilde{u}_x \tilde{u}_z}}{\partial z} = \frac{D_{\text{bf}}\,\cos\phi}{\rho\,c_w\,\delta}\left(1 - \frac{h-z}{\delta}\right)\bigg|_{h-\delta<=z<=h}, \tag{7}$$

where $\tilde{u}_x$ and $\tilde{u}_z$ are the horizontal and vertical components of the orbital velocity, D_{bf} is the wave energy dissipation by bed friction, ϕ is the wave direction, and c_w is the wave phase velocity. The total wave force resulting from the gradients in radiation stress is divided into a part related to wave surface dissipation, and into wave body forces, following Dingemans et al. (1987).

Following Reyns et al. (2023), the bed shear stress $\boldsymbol{\tau_b}$ due to currents and waves can be modelled using the approach of Soulsby et al. (1993) which parametrizes various wave–current interaction models to establish the combined bed shear stress effect, or by using Ruessink et al. (2001). When using the van Rijn (2007a,b,c) sediment transport formulations, we derive the value of the bed shear stress as a function of the apparent bed roughness, which is a non-linear function of bedform height, wave non-linearity and flow velocity, as described in van Rijn (2007a). In all approaches, the bed shear stress is established from the Eulerian velocity vector in the near-bed σ layer.

To model the anisotropic turbulence, we separate horizontal and vertical spatial scales, and apply the eddy viscosity concept (Prandtl, 1905). Horizontal diffusion of momentum is modelled using a user-specified dynamical viscosity coefficient ν_h and Smagorinsky subgrid turbulence (Smagorinsky, 1963) to handle unresolved horizontal mixing. In this study, the vertical viscosity ν_z is modelled using a zero or two equation turbulence model. For models featuring uniform flow without waves and wind, we use the algebraic turbulence model (Eq. (8)):

$$\nu_z = \kappa z(1 - z/h)u_{*,b}, \tag{8}$$

where κ is the von Kármán constant; z is the height from the bed; and $u_{*,b}$ is the bed friction velocity, calculated as $\kappa|\boldsymbol{u}_b|/\ln((\delta(z_b) + 9\ z_0)/(e z_0))$, where $|\boldsymbol{u}_b|$ is the velocity magnitude in the bottom layer, $\delta(z_b)$ is the bottom layer thickness, e is the base of the natural logarithm, and z_0 is the roughness height. Applying the algebraic turbulence model gives rise to a logarithmic velocity profile. Although algebraic turbulence models exist for wave–current interaction (e.g., Tambroni et al. (2015)), we calculate the vertical viscosity in the non-uniform cases presented in Section 4 from

$$\nu_z = c_\mu\,\frac{k^2}{\epsilon} \tag{9}$$

using the $k-\epsilon$ model of Jones and Launder (1972), with additions to account for wave influences in the production terms (Walstra et al., 2001; Le, 2012) and buoyancy effects for stratified flows (Rodi, 1993):

$$\frac{\partial k}{\partial t} + \nabla\cdot(\boldsymbol{u}\,k) + \frac{\partial u_z\,k}{\partial z} = \frac{\partial}{\partial z}(\nu_{z,k}\frac{\partial k}{\partial z}) + P_k + B_k - \epsilon \tag{10}$$

$$\frac{\partial \epsilon}{\partial t} + \nabla\cdot(\boldsymbol{u}\,\epsilon) + \frac{\partial u_z\,\epsilon}{\partial z} = \frac{\partial}{\partial z}(\nu_{z,\epsilon}\frac{\partial \epsilon}{\partial z}) + c_{1\epsilon}\,\nu_z\,\frac{\epsilon}{k}\left(P_k + (1 - c_{3\epsilon})B_k\right) - c_{2\epsilon}\,\frac{\epsilon^2}{k}, \tag{11}$$

where k is the kinetic energy, t is time, ϵ is the rate of turbulent energy dissipation, B_k is the buoyancy-related flux of k, equal to $g\,\nu_z\,/(\rho\sigma_\rho)\,\frac{\partial \rho}{\partial z}$; $\nu_{z,k}$ is the sum of the kinetic viscosity and ν_z/σ_k, with $\sigma_k = 1.0$; $\nu_{z,\epsilon}$ equals ν_z/σ_ϵ, with $\sigma_\epsilon = 1.3$. σ_ρ is the Prandtl-Schmidt number, equal to 0.7 for salt and temperature, and 1.0 for suspended sediment.

c_μ, $c_{1\epsilon}$, $c_{2\epsilon}$ are calibration constants with values 0.09, 1.44 and 1.92, respectively (Launder and Spalding, 1972). $c_{3\epsilon}$ is 0.0 in case of unstable stratification, else it is equal to 1.0 (Rodi, 1987). The kinetic energy production term in the water column P_k contains contributions of the vertical shear of the horizontal Eulerian velocities (Ardhuin and Jenkins, 2006), and of turbulence generation due to wave and roller energy dissipation (Nguyen et al., 2021; Le, 2012):

$$P_k(z) = \nu_z(z)\left|\frac{\partial \boldsymbol{u}^E(z)}{\partial z}\right|^2 + \frac{2\ D_{w,r}}{\rho\ \alpha_{\text{wave}} H_{rms}}\left(1 - \frac{h-z}{\alpha_{\text{wave}} H_{rms}}\right)\Bigg|_{h-\alpha_{\text{wave}} H_{rms} <= z < h}, \tag{12}$$

where $\boldsymbol{u}^E$ is the horizontal Eulerian velocity field, z is the height above the bed, $D_{w,r}$ is the energy dissipation by whitecapping, wave breaking and surface rollers (Feddersen and Trowbridge, 2005), H_{rms} is the RMS wave height, and α_{wave} is a parameter controlling the depth over which the dissipation is distributed (Moghimi et al., 2016; Feddersen, 2012). The equations are subject to bed and surface boundary conditions (Le, 2012):

$$k|_{z=\text{bed}} = \frac{u_{*,b}^2}{\sqrt{c_\mu}}, \qquad k|_{z=\text{surface}} = \frac{u_{*,w}^2}{\sqrt{c_\mu}} + \left(\frac{\kappa\ D_{w,r}}{30\rho c_{de}}\right)^{2/3} \tag{13}$$

$$\left.\frac{\partial \epsilon}{\partial z}\right|_{z=\text{bed}} = -\frac{u_{*,b}^3}{\kappa\ (\delta(z_b)/2 + 9z_0)^2}, \qquad \left.\frac{\partial \epsilon}{\partial z}\right|_{z=\text{surface}} = \frac{u_{*,w}^3}{\kappa\ (\delta(z_s)/2)^2} + \frac{2D_{w,r}}{\rho\,(\alpha_{\text{wave}} H_{rms})^2}, \tag{14}$$

where κ is the von Kármán constant, $u_{*,w}$ is the wind friction velocity, equal to $\sqrt{f_{wd}\frac{\rho_a}{\rho}}|\boldsymbol{u_w}|$; $u_{*,b}$ is the bed friction velocity, c_{de} is a calibration constant equal to $c_\mu^{3/4}$, z_0 is the roughness height, $\delta(z_b)$ is the bottom layer thickness, and $\delta(z_s)$ is the top water layer thickness.

2.2. Sediment transport and morphological updating

We model multi-fraction total sediment transport as the sum of bedload and suspended load over the fractions (van Rijn, 1993):

$$\boldsymbol{q}_{\text{tot}} = \sum_{nf}\left(\kappa_{\text{bed}}\,\boldsymbol{q}_{\text{i,bed}} + \int_a^h \boldsymbol{q}_{\text{i,sus}}\,\mathrm{d}z\right), \tag{15}$$

where $\boldsymbol{q}_{\text{tot}}$ is the total transport vector, nf is the number of fractions, $\boldsymbol{q}_{i,bed}$ is the bedload vector for fraction i, $\boldsymbol{q}_{\text{i,sus}}$ is the suspended load vector, κ_{bed} is a proportionality factor, and a is the height above the bed where the reference concentration is calculated to determine the source term for the suspended transport. We assume that all bedload transport occurs below a. In our model, we distinguish four types of sediment fractions, which determine the allowable type of transport for the fraction under consideration. The clay (d_{50} <=32 μm) and silt fractions (32 μm< d_{50} <=64 μm) are only transported as suspended load, and the sand fractions (64 μm < d_{50} <=2000 μm) can be transported as combined bedload and suspended load. Lastly, gravel fractions (d_{50} >2000 μm) are modelled as bedload only. The interaction of multiple (cohesive and/or non-cohesive) sediment fractions can be taken into account in the critical bed shear stress for the initiation of motion (e.g. van Rijn, 2007a), in the bed shear stress used for cohesive transport (Soulsby and Clarke, 2005), in the source terms for suspended sediment transport (van Ledden, 2002), and in the bed composition model (Section 2.2.4). In the model's GLM framework, we use different velocity definitions to calculate bedload and suspended fluxes. Near the bed, the bed shear stress is modelled using the instantaneous velocity, and wave effects are taken into account using contributions derived from the wave orbital velocity (e.g., Soulsby et al., 1993). As bed load transport is closely related to dissipation in the bottom boundary layer, we use the same instantaneous velocity estimate, i.e. the Eulerian velocity, to estimate the bed load transport vector, as well as the reference concentration that serves as the bed boundary condition for suspended transport. In contrast, fluid mass propagates with the Lagrangian velocity, which accounts for the short wave-related phase-averaged mass flux (Stokes drift) in addition the mean current velocity in a consistent set of equations. Any matter that is transported in the water column, including suspended sediment, is hence transported with this velocity.

2.2.1. Bedload sediment transport

Sediment transport vectors (Section 2.2.3) are determined in the cell centres, and subsequently projected in the face-normal direction on the cell faces using an upwind approach that is similar to the procedure described by Lesser et al. (2004). After establishment of the bedload vector in the cell face position, we apply longitudinal and transversal bed slope effects to the vector magnitude and direction (Bagnold, 1966; Ikeda, 1982). If we denote the bed slope in the uncorrected bedload transport direction as σ_s, and the slope perpendicular to it, σ_n, then the corrected bedload vector $\boldsymbol{q}_{\text{bed,c}}$ equals:

$$\boldsymbol{q}_{\text{bed,c}}^{\text{lon}} = \left(1 + \alpha_{bs}\,\frac{\tan\phi}{\cos\left(\arctan\sigma_s\right)\left(\tan\phi - \sigma_s\right)}\right)\boldsymbol{q}_{\text{bed}}, \tag{16a}$$

$$\boldsymbol{q}_{\text{bed,c}} = \boldsymbol{q}_{\text{bed,c}}^{\text{lon}} + \alpha_{bn}\sqrt{|\boldsymbol{\tau}_{b,cr}|/|\boldsymbol{\tau}_{b,wc}|}\,\sigma_n\left(\hat{\boldsymbol{e}}_z \times \boldsymbol{q}_{\text{bed,c}}^{\text{lon}}\right), \tag{16b}$$

where $\boldsymbol{q}_{\text{bed}}$ is the uncorrected bedload vector, $\boldsymbol{q}_{\text{bed,c}}^{\text{lon}}$ is the bedload vector corrected for longitudinal slope effects, α_{bs} and α_{bn} are calibration factors, $\hat{\boldsymbol{e}}_z$ is the unit vector in the z direction, and ϕ is the sediment repose angle.

2.2.2. Suspended sediment transport

Transport of suspended sediment is calculated by solving the 3D advection-diffusion equation with a source and a settling term per sediment fraction. Only clay, silt and sand can be modelled as suspended fractions, and their type and abundance will determine the applied formulations for the settling velocity and the source terms. The 3D advection-diffusion equation reads

$$\frac{\partial c}{\partial t} + \nabla\cdot(\boldsymbol{u}c) + \frac{\partial}{\partial z}\left(\left(u_z - |w_s|\right)c\right) - \nabla\cdot\left(\epsilon_h\cdot\nabla c\right) - \frac{\partial}{\partial z}\left(\epsilon_{wc}\frac{\partial c}{\partial z}\right) = E - D \tag{17a}$$

$$E = \epsilon_{ws,\text{bed}}\left.\frac{c_a - c}{\delta(z_b)}\right|_{z=\text{bed}} \tag{17b}$$

$$D = \left.\frac{w_s\,c}{\delta(z_b)}\right|_{z=\text{bed}}, \tag{17c}$$

where c is the sediment concentration, t is time, z is the vertical coordinate, ϵ_h is the horizontal sediment diffusivity parameter, ϵ_{wc} is the vertical sediment diffusivity, E and D are the sediment source and sink terms for sand, respectively, c_a is the reference concentration, and $\delta(z_b)$ is the layer thickness at the bed. The settling velocity of sand fractions w_s is calculated using the formulations of van Rijn (2007b) by default, which incorporate hindered settling (Richardson and Zaki, 1954) and simplified flocculation. More advanced flocculation models (Manning and Dyer, 2007; Chassagne and Safar, 2020) can be applied for cohesive fractions, overruling the default fraction-specific, user-defined, constant settling velocity. For cohesive fractions, D and E are calculated following Krone (1962) and Partheniades (1965), and the presence of a thin muddy buffer layer influencing E can be taken into account using the concepts presented by Van Kessel et al. (2011).

2.2.3. Sediment transport formulations

Although a multitude of transport formulations are available in Delft3D-FM (Deltares, 2025b), in this study (Section 4) we only use the transport relations of van Rijn (2007a,b,c), the transport formulations of van Thiel-van Rijn (Roelvink et al., 2009), and the bedload transport relation of Meyer-Peter and Müller (1948), depending on the various applications in Section 4. In the following, we provide an outline of these transport formulae, and refer to the original publications for more details.

TRANSPOR2004 transport relations. The TRANSPOR2004 sediment transport formulations (van Rijn, 2007a,b,c; Walstra et al., 2007) provide estimates of bed roughness, a reference concentration c_a at reference height a for the advection-diffusion equation, of wave- and current-driven bedload transport below the reference height, and of suspended load due to the presence of waves in the suspension layer δ_{sus}. Together, they provide a framework to estimate the total sediment transport under the combined action of currents and waves.

van Rijn discerns contributions to the bed shear stress by skin friction, and by form drag of ripples, megaripples and dunes. The dimensions of these bedforms are a function of local water depth h, sediment grain size and the mobility parameter $\psi = (|\boldsymbol{u}|_c^2 + |\boldsymbol{u}|_{orb}^2)/[(\rho_s/\rho - 1)\, g\, d_{50}]$, expressing the balance of forces acting on sediment grains (van Rijn, 2007a). Here, ρ_s is the specific density of the sediment fraction under consideration, $\boldsymbol{u}_c$ is the depth-averaged current vector, based on a logarithmic velocity profile reconstruction, and $\boldsymbol{u}_{orb}$ is the representative peak orbital velocity vector, derived from Isobe and Horikawa (1982). When the ripple height k_{sr} is known, a is established as $a = k_s/30 + 0.5\, k_{sr}$, with k_s the grain-related roughness, for both current only and combined wave–current induced flow (van Rijn, 2007a). The critical bed shear stress $\boldsymbol{\tau}_{b,cr}$ is established based on van Rijn (1993), with modifications for fine sand by van Rijn (2007a).

The total wave-averaged bedload transport vector $\boldsymbol{q}_{\text{bed}}$, consisting of the sum of wave and current-related contributions, is calculated from reconstructed intra-wave time series $\boldsymbol{u}_{wc}^E$ at height a, based on Isobe and Horikawa (1982), Albernaz et al. (2019), and Nielsen (1992):

$$\boldsymbol{q}_{\text{bed}} = \frac{1}{T_p}\int_0^{T_p} \frac{\boldsymbol{u}_{wc}^E}{|\boldsymbol{u}_{wc}^E|}\,|\boldsymbol{q}_{b,wc,\text{inst}}|\,\mathrm{d}t \tag{18a}$$

$$\boldsymbol{q}_{\text{bed,c}} = \frac{1}{T_p}\int_0^{T_p} \frac{\boldsymbol{u}_{c}^E}{|\boldsymbol{u}_{wc}^E|}\,|\boldsymbol{q}_{b,wc,\text{inst}}|\,\mathrm{d}t \tag{18b}$$

$$\boldsymbol{q}_{\text{bed,w}} = \boldsymbol{q}_{\text{bed}} - \boldsymbol{q}_{\text{bed,c}} \tag{18c}$$

$$\boldsymbol{q}_{\text{bed,wc,inst}} = 0.5\,\rho_s\, f_{\text{silt}}\, d_{50}\, D_*^{-0.3} \sqrt{\boldsymbol{\tau}_{b,wc}/\rho}\,\left[(\boldsymbol{\tau}_{b,wc} - \alpha_{\text{im}}\,\beta_{\text{slp}}\,\boldsymbol{\tau}_{b,cr})/(\beta_{\text{slp}}\boldsymbol{\tau}_{b,cr})\right], \tag{18d}$$

where $\boldsymbol{q}_{\text{bed,wc,inst}}$ is the instantaneous total bed load transport vector, T_p is the peak wave period, $\boldsymbol{u}_c^E$ is the non-oscillatory part of the velocity signal, $\boldsymbol{q}_{\text{bed,c}}$ is the wave-averaged current-related bed load transport vector, $\boldsymbol{q}_{\text{bed,w}}$ is the wave-averaged wave-related bed load transport vector, f_{silt} is $\max(6.2\times10^{-5}/d_{50}, 1)$, $D_* = d_{50}\left((s-1)g/\nu^2\right)^{1/3}$ is the dimensionless grain size, s is the relative density, g is the gravitational acceleration, ν is the kinematic viscosity, $\boldsymbol{\tau}_{b,wc}$ is the instantaneous grain-related bed shear stress due to currents and waves (van Rijn, 2007a), α_{im} is a factor to account for the stochastic character of the initiation of motion (van Rijn, 2006), and β_{slp} accounts for the bed slope effect on the critical shear stress (Dey, 2003; Walstra et al., 2007).

The near-bed sediment transport vector $\boldsymbol{q}_{s,w}$ in the suspension layer δ_{sus}, driven by asymmetric oscillatory wave motions is given by van Rijn (2007b):

$$\boldsymbol{q}_{s,w} = \boldsymbol{u}_a \int_a^{\delta_{\text{sus}}} c\,\mathrm{d}z \tag{19a}$$

$$\delta_{\text{sus}} = 2.16\,(1 + \sqrt{H_s/h - 0.4})\, A_\delta (k_{sr}/A_\delta)^{1/4}, \tag{19b}$$

where c is the sediment concentration, $\boldsymbol{u}_a = 0.1\,\alpha_{\text{pl}}\,(u_{\text{on}}^4 - u_{\text{off}}^4)/(u_{\text{on}}^3 + u_{\text{off}}^3)$ is the wave-averaged drift velocity resulting from wave non-linearity (Isobe and Horikawa, 1982; Albernaz et al., 2019), α_{pl} is the phase-lead function that accounts for the phase shift between shear stress and sediment mobilization (Walstra et al., 2007), H_s is the significant wave height, and A_δ is wave orbital excursion. Although conceptually not entirely correct, this transport contribution is modelled as a bedload flux in our model.

Suspended sediment transport due to mean currents is modelled by solving a 3D advection diffusion equation (Section 2.2.2), which requires a sediment concentration c_a at the reference height a to construct the source terms, and the vertical distribution of the sediment diffusivity profile ϵ_{wc}.

$$c_a = \kappa_{\text{sus}}\, 0.015\,(1 - p_{\text{clay}})\, f_{\text{silt}}\, \frac{d_{50}}{a}\, D_*^{-0.3}\, T^{1.5}, \tag{20}$$

where κ_{sus} is a user-defined proportionality factor, p_{clay} is the percentage of clay in the total sediment mixture in the transport layer, and $T = \left[(\boldsymbol{\tau}_{b,wc} - \alpha_{\text{im}}\,\beta_{\text{slp}}\,\boldsymbol{\tau}_{b,cr})/(\beta_{\text{slp}}\boldsymbol{\tau}_{b,cr})\right]$ is the dimensionless excess shear stress, established from the wave-averaged, depth-averaged current and the peak orbital velocity (van Rijn, 2007a,b). The sediment diffusivity profile is calculated per fraction as $\epsilon_{wc}(z) = \sqrt{\epsilon_c^2(z) + \epsilon_w^2(z)}$ (van Rijn, 1993), and assuming that the Prandtl-Schmidt number equals 1.0 for non-cohesive fractions and 0.7 for cohesive sediment. van Rijn (1984) accounts for the difference in dispersion behaviour of sediment and water in the current-related mixing, using a factor $\beta_{\text{mix}} = 1 + (w_s/u_{*,c})^2$, where w_s is the settling velocity, incorporating flocculation and hindered settling effects (van Rijn, 2007b), and $u_{*,c}$ is the current-related shear velocity. When using the algebraic turbulence model (Section 2.1), ϵ_c and ϵ_w have parametrized shapes. The current-related mixing parameter ϵ_c has a parabolic-constant form, and the wave-related diffusivity parameter is a piecewise-linear function (van Rijn, 1993). In the case of using the $k-\epsilon$ turbulence model, the eddy diffusivity is converted to a sediment diffusivity parameter by multiplication with a factor $\beta_f = 1 + (\beta_{\text{mix}} - 1)\,\boldsymbol{\tau}_c/(\boldsymbol{\tau}_c + \boldsymbol{\tau}_w)$, so that it only affects the current-related mixing, as intended by van Rijn (1984).

van Thiel/van Rijn (Roelvink et al., 2009). In order to model erosion hazards on sandy beaches during extreme events, the XBeach model (Roelvink et al., 2009) contains an adapted version of the Soulsby-van Rijn transport formula (Soulsby, 1997) by adding the influence of roller-generated turbulence to the orbital velocity estimate, and recalibrating the transport coefficients (van Thiel de Vries, 2009), by calculating the settling velocity, including hindered settling, according to Ahrens (2000), by considering the effect of dilatancy to reduce sediment mobilization (De Vet et al., 2015), and by incorporating bed slope effects to the transport estimates and the critical bed shear stress (Walstra et al., 2007). Velocity contributions due to wave non-linearities are derived based on Abreu et al. (2010) and Ruessink et al. (2012).

In our model application (Section 4.3.4), we include the bedload related part of the total transport as an explicit bedload flux, and we derive a reference concentration for the 2D advection-diffusion equation to model the suspended part of the sediment load, incorporating the proportionality factor κ_{sus}, similarly to Eq. (20). We use the settling velocity formulation of van Rijn (1993) and the formulations of Galappatti and Vreugdenhil (1985) to derive the suspended sediment source terms. We omit the bed slope effects on the transport magnitude and direction as used in XBeach, but apply the standard adjustments for downslope transport (Bagnold (1966), Ikeda (1982), see Section 2.2.1). The wave non-linearity contribution to the velocity $\boldsymbol{u}_a$ is omitted for the suspended transport. The bedload transport $\boldsymbol{q}_{\text{bed}}$ and the reference concentration c_a are then given by:

$$\boldsymbol{q}_{\text{bed}} = \rho_s\, \frac{A_b}{h}\,(|\boldsymbol{u}_{\text{tot}}| - u_{\text{cr}})^{1.5}(\boldsymbol{u}^E + \boldsymbol{u}_a)\mathcal{H}\left(|u_{\text{tot}}| - u_{\text{cr}}\right) \tag{21a}$$

$$c_a = \kappa_{\text{sus}}\,\rho_s\, \frac{A_s}{h}\,(|\boldsymbol{u}_{\text{tot}}| - u_{\text{cr}})^{2.4}\mathcal{H}\left(|u_{\text{tot}}| - u_{\text{cr}}\right), \tag{21b}$$

where A_b and A_s are the bed load coefficient, and the suspended load coefficient, respectively (van Thiel de Vries, 2009), which are functions of the grain size, relative density of the sediment and the local water depth; u_{cr} is the critical velocity magnitude for sediment mobilization, $\boldsymbol{u}_{\text{tot}} = \sqrt{(\boldsymbol{u}^E)^2 + 0.64\,(u_{\text{rms}}^2 + 1.45\,k_b)}$ is the stirring velocity vector, u_{rms} is the RMS orbital velocity magnitude, k_b is the roller turbulence contribution to the stirring, and $\mathcal{H}$ is the Heaviside function (van Thiel de Vries, 2009).

Bedload formula of Meyer-Peter and Müller (Meyer-Peter and Müller, 1948). The Meyer-Peter and Müller (1948) sediment transport relation gives an estimate for the bedload as follows:

$$\boldsymbol{q}_{\text{bed}} = 8\, d_{50} \sqrt{\frac{(\rho_s - \rho)}{\rho}\, g\, d_{50}} (\mu_r\, \theta - 0.047)^{3/2}, \tag{22}$$

where $\mu_r = \left(C/C_{\text{d90}}\right)^{3/2}$ is the ripple factor, C is the total drag Chézy parameter, C_{d90} is the grain-related Chézy parameter, and θ is the Shields mobility parameter, derived using the total drag. In our application, we ignore the influence of hiding/exposure on the critical bed shear stress.

2.2.4. Bed composition and morphological updating

Bed composition. When using multiple sediment fractions, it becomes important to keep track of the vertical distribution of the different sediment fractions in the bed, as layers of easily erodible sediments may alternate with more erosion-resistant layers as a result of time- and space varying erosional and depositional processes. In order to model the layered bed composition, we follow the concepts first elaborated by Hirano (1971), where the bed is divided into a well-mixed top-most active layer and a set of substrate layers, of which the mass distribution is tracked in time. Erosion and deposition, resulting from transport processes described earlier (Section 2.2.3), change the mass of the active layer. Substrate layers below the active layer do not exchange sediment with the water column directly, but their composition will be affected by the scour or replenishment of the active layer. The temporal change in mass per unit area m_{al} of the active layer is given by:

$$\frac{\partial m_{\text{al}}}{\partial t} = -\alpha_{\text{MF}} \sum_{\text{i}=1}^{\text{nf}} \left(\nabla \cdot \boldsymbol{q}_{\text{bed,i}} - D_{\text{i}} + E_{\text{i}} - m_{\text{dd,i}} + \rho_{s,\text{i}}\, \phi_{\text{al,i}}\, \frac{d z_{\text{al}-1}}{dt} \right), \tag{23}$$

where subscript i indicates a fraction-dependent quantity, α_{MF} is the morphological acceleration factor, D_{i} is the deposition flux, E_{i} is the erosion flux, $m_{\text{dd,if}}$ is the nett mass change resulting from dredging and dumping operations, $\rho_{s,\text{i}}$ is the specific density, $\phi_{\text{al,i}}$ is the volumetric fraction, where $\sum_{i=1}^{nf} \phi_{\text{al,i}} = 1 - \lambda_p$, with λ_p the bed porosity. The term $d z_{al-1}/dt$ is the velocity of the interface between the active layer and the first substrate layer below it. In the default configuration, the active layer has a constant thickness, and mass is transferred between the active layer and the first substrate layer to accommodate for scour and aggradation. The first substrate layer under the active layer can change its thickness in time by receiving from or providing mass to the active layer. The thickness of the substrate layers below that layer is constant. If, in the case of deposition, the maximum allowed layer thickness is reached for the first substrate layer, a new substrate layer is created above the original one. Similarly, in case of complete erosion of the first substrate layer, the original second substrate layer becomes the layer that exchanges mass with the active layer. Mass change $\partial m_1/\partial t$ of the first substrate layer then equals:

$$\frac{\partial m_1}{\partial t} = \alpha_{\text{MF}} \sum_{\text{i}=1}^{\text{nf}} \left(\rho_{s,\text{i}}\, \phi_{1,\text{i}}\, \frac{d}{dt}(z_b - \delta_{\text{al}}) \right), \tag{24}$$

where z_b is the bed level, and δ_{al} is the active layer thickness. If the creation of a new substrate layer would exceed the maximum allowed number of substrate layers, layers at the bottom of the stratigraphy stack will be merged.

Morphological updating. The change in sediment mass is translated into a bed level change based on the bed porosity λ_p and the specific densities of the various sediment fractions $\rho_{s,\text{if}}$. The bed level change $\partial z_b/\partial t$ is given by

$$\frac{\partial z_b}{\partial t} = \frac{\partial z_{b,0}}{\partial t} + \frac{\partial \delta_{\text{all}}}{\partial \lambda_p} \frac{\partial \lambda_p}{\partial t} + \sum_{\text{i}=1}^{\text{nf}} \frac{\partial \delta_{\text{all}}}{\partial m_{\text{all,i}}} \frac{\partial m_{\text{all,i}}}{\partial t}, \tag{25}$$

where $\partial z_{b,0}/\partial t$ is the 'background' base substrate level change by e.g. subsidence, δ_{all} is the total sediment thickness, and $m_{\text{all,i}}$ is the total mass of fraction i in the stratigraphy stack. In this paper, we ignore the change in porosity in our applications.

In addition to the standard bed update procedure from spatial sediment transport gradients, we consider two extra mechanisms in our model that change the local bed level. During collision regime conditions in coastal storms (Sallenger, 2000), when waves actively impact on the dune front, dune face slumping is the dominant erosion mechanism (van Thiel de Vries et al., 2008; Palmsten and Holman, 2012). This process is triggered in the model when the slope between two adjacent cells is steeper than a critical value σ_c. The cell face-normal flux q_{av} required to re-establish the critical slope is included as an additional downslope bedload transport component, with linear relaxation over a predefined avalanching period T_r. After taking into account the relative availability of different sediment fractions, this flux is added to the transport flux divergence contribution to the bed update, ensuring mass conservation.

$$q_{\text{av}} = \sum_{\text{i}=1}^{\text{nf}} \frac{\rho_{s,\text{i}}\, \phi_{\text{i}}\, w}{\alpha_{\text{MF}} T_r} \frac{S_1\, S_2}{S_1 + S_2} \left(z_{b,1} - z_{b,2} + \sigma_c \mathrm{d}s \right) \mathcal{H}\left(\left| \frac{\partial z_b}{\partial s} \right| - \sigma_c \right), \tag{26}$$

where S_1 and S_2 are the areas of the two cells sharing the cell face under consideration, $z_{b,1}$ and $z_{b,2}$ are the corresponding bed levels, w is the cell face width, $\mathrm{d}s$ is the distance between the cell centres of cells 1 and 2, and $\partial z_b/\partial s$ is the total bed slope in the face-normal direction. On longer time scales of weeks to months, the swash zone of beaches tends to recover to a certain stable cross-shore slope, which depends roughly on wave exposure, the median grain size and sediment sorting (Wiegel, 2005; Reis and Gama, 2010; McFall, 2019). Based on these findings, Roelvink and Costas Otero (2017), Roelvink et al. (2019) postulated that post-storm beach recovery could be incorporated in process-based models by nudging the swash zone slope to a predefined value. This slope value can be derived from field observations, or from literature. In our model, this process is again incorporated as an additional bedload flux q_{sl} in cell face-normal direction. It is constrained in space to the inner surf zone, by setting a critical depth and breaker parameter value $\gamma_{\text{br,c}}$. We assume that the local wave direction is a good proxy for the orientation of the maximum bed slope, so we get for the sediment flux q_{sl}:

$$q_{\text{sl}} = \alpha_{\text{cal}} \sum_{\text{i}=1}^{\text{nf}} \left| \boldsymbol{q}_{\text{bed,if}} \right| \left(\frac{\partial z_b}{\partial s} - \sigma_{\text{bs}}\, \frac{k_n}{|\boldsymbol{k}|} \right) \mathcal{H}\left(\frac{H_{\text{rms}}}{h} - \gamma_{\text{br,c}} \right), \tag{27}$$

where α_{cal} is a calibration factor, $\partial z_b/\partial s$ is the local bed slope in the face-normal direction, σ_{bs} is the slope magnitude to nudge towards, $\boldsymbol{k}$ is the wave number vector, k_n is the wave number component in the direction of the face normal vector, and $\gamma_{\text{br,c}}$ is the critical wave breaker parameter.

In order to speed up the morphological simulations, the changes in sediment mass can be multiplied with a morphological acceleration factor (Roelvink, 2006), which can change over the time of the simulation. For models where the hydrodynamic forcing can be schematized in a set of representative conditions, our model allows for the application of the parallel online method (Roelvink, 2006), where the morphodynamic evolution of the study area is determined based on the concurrent calculation and weighted averaging of the bed updates. This allows for morphological runs over time periods from hours to years with reasonable run times.

3. Numerical implementation

In the horizontal plane, the orthogonal unstructured grid is discretized using a hybrid combination of triangles and/or quadrilateral curvilinear parts. In the vertical, we discretize the domain using terrain-following σ coordinates. The model is completely parallelized using the Message Passing Interface (MPI) protocol, and it is Basic Model Interface (BMI) compatible (Hutton et al., 2020), allowing for flexible in-memory communication with other model frameworks.

3.1. Hydrodynamics

The horizontal advection and diffusion terms for momentum (Eq. (4)) are discretized in the cell centres, interpolated back to the cell faces (Perot, 2000), and reprojected in face-normal orientation. The horizontal advection term is discretized using a higher-order, total variation diminishing (TVD) limited upwind scheme. Coriolis terms are discretized in an energy-conserving way following Kleptsova et al. (2009). Vertical advection of momentum is discretized with a first-order upwind approach. The turbulence equations are solved implicitly in a decoupled fashion, using first-order upwind discretizations for horizontal advection and vertical advection and diffusion.

Time integration of the shallow water equations is performed using a predictor–corrector approach (Martyr-Koller et al. (2017), eqn. A9-A11), where the explicit time integration of the advection part gives rise to a time step restriction (Table 1). Based on the velocities from the predictor step, the water level equation is solved implicitly. The final velocities for the time step are back-calculated from the updated water levels. In order to accommodate drying and flooding, cell faces with a water depth smaller than a user-defined threshold value at the beginning of a time step are removed from the numerical system that is solved. If the water level of a cell becomes lower than the bed level during the implicit time integration, the faces belonging to that cell are deactivated, and the time step is repeated. The water depth and the face-normal velocities for these faces are zero in the next time step (Deltares, 2025a).

3.2. Sediment transport and morphology

In order to simplify the solution procedure, the bed level updating is decoupled from the solution of the hydrodynamic equations, which is a reasonable assumption for low to moderate Froude numbers (Morris and Williams, 1996; Lyn and Altinakar, 2002). Updating of the bed levels requires estimates of the bedload transports (including van Rijn's suspended transport by waves), and of the suspended sediment erosion and deposition fluxes, per sediment fraction in the model. All sediment transport quantities are computed in the cell centres. In order to calculate the transport divergence (Eq. (23)), the bedload vectors are transposed from the cell centres to the cell faces using an upwinding approach. In this approach, the upwind cell, which provides the bedload vector, is determined from the transport direction in the face-adjacent cell centres (Lesser et al., 2004). For sediment transport models that do not provide an estimate for the reference height a, the source and sink terms for the advection-diffusion solver (Eq. (17c)) are imposed in the first vertical layer above the bed. For non-zero reference heights, the first layer completely above a is used. The source and sink terms are then determined from the reference concentration value and the present concentration value by vertical interpolation, assuming a Rouse concentration profile (Deltares, 2025b). The source terms are modelled explicitly, and the sink terms are added implicitly. In order to account for double counting of the bed load and suspended load below a, an optional correction vector can be added to the transport divergence term in the bed mass update equation (Lesser et al., 2004). To preserve and track mass conservation, we implemented the following features. When the bed level of a cell changes after the morphological update, the volume of the local water column changes. This volume change is accounted for in an increase of the concentration of matter. In areas where the available total sediment thickness h_{sed} is less than a predefined critical value $h_{sed,c}$, and erosive conditions are expected, the bed load transport magnitude, and the source and sink terms are reduced with a factor $h_{sed}/h_{sed,c}$. If the eroded volume is larger than the amount of available sediment, this shortage is tracked. Subsequent deposition is used to reduce this volume deficit first. The suspended sediment volume in cells that become dry in a time step is tracked in a separate array as well. Upon renewed flooding of the cell, the volume is accounted for in the deposition flux for that new time step. The advection and diffusion terms for suspended sediment are discretized in the cell centres, using the same higher-order TVD limited upwind scheme as used in the momentum advection, both in the horizontal and in the vertical. The contribution by the settling flux in the water column is discretized implicitly, due to its severe impact on the maximum allowed time step. The time integration of the advection-diffusion equation solver for suspended sediment concentration is explicit, and in general, this puts a more severe limit on the explicit time step than the time integration in the momentum solver does (Table 1). This is alleviated by using a local time stepping mechanism, that allows the solution in different parts of the computational domain to advance with varying time steps based on local CFL_{max} numbers, improving efficiency while maintaining overall stability and accuracy (Sanders, 2008).

4. Model verification

In this section, we present a number of 2D and 3D test cases to verify the implementation of the formulations described in Section 2. First, we present two verification cases for velocity profiles under wave–current interaction in the cases of breaking and non-breaking waves. Next, we look at the conservation of sediment mass and the build-up of concentration profiles in the presence and absence of waves. Lastly, we present a number of cases where we verify different aspects of morphodynamic updating described in Section 2.2.4.

4.1. Wave-driven hydrodynamics

4.1.1. Currents under non-breaking waves

In order to investigate the vertical structure of the mean flow driven by conservative wave forcing under wave–current interaction on a horizontal bed, Klopman (1994) performed a series of tests in the 46m long combined wave–current Scheldt flume of WL|Delft Hydraulics. The flume had wave boards at either end capable of active absorption of incoming waves. The experiment consisted of runs with regular, bichromatic and random waves following and opposing a current, and wave propagation without the presence of a current. The water depth was set at 0.5m above the built-in wooden flume floor, and wave and flow conditions were imposed according to the values in Table 2. Wave steering was performed using second-order Stokes theory. The current was generated by a 0.8 $m^3 s^{-1}$ discharge, generated by a pump in the flume bed. Here, we replicate the test series with random waves, of which the ensemble averaged results for the mean flow structure are depicted in Fig. 1. We identify the experiments with following, opposing and no current with WFC, WOC and WNC, respectively. The case without waves is denoted as CNW.

In order to reproduce the measurements, an online coupled flow-wave model was set up, using SWAN (Booij et al., 1999) as the wave driver to replicate the random wave field. The coupling interval was set at 240 s. The domain was discretized using a resolution of 0.5m in the horizontal, using a 2016 cell curvilinear grid for the wave model, and an unstructured grid with 184 cells for the flow model. In the flow model, our base model was defined with 40 uniform σ layers in the vertical. Using a combination of upstream total discharge and downstream water level boundaries, uniform flow was generated in the flume, and verified using a run without wave forcing (CNW, Fig. 1). The current-related bed roughness was parametrized using the White-Colebrook formulation (Colebrook and White, 1937), by specifying a roughness height k_s. Without waves, the best fit to the flow profile was obtained using a value of 8×10^{-5} m. Klopman (1994) states that this value should be a factor 2–4 smaller in the case when waves are present, and here, we used 4×10^{-5} m. Spatially uniform, stationary wave conditions were imposed according to the values in Table 2. All other parameters were left at their default values (Table A.1).

In the upper half of the water column, results show that waves opposing (WOC) and following a current (WFC) cause bending of the flow profile in the direction of, or against the current, respectively (Fig.

Table 1
Time step criteria applied in the explicit part of the time integration in Delft3D-FM. Δt^{n+1}: time step size at new time level $n+1$; $\mathrm{CFL}_{\max}$: maximum CFL number; V^n: cell volume at old time level n; Q^n_{out}: outgoing volume flux of cell at old time level; Q^n_{in}: incoming volume flux of cell at old time level; S_{cell}: cell surface area; $(\Delta z_b)_{\max}$: user defined maximum allowed bed level change per time step; Q^n_{sed}: total outgoing face-normal sediment discharge in a cell at old time level; w: width of a cell face; ${c_g}^n$: outgoing face-normal wave group velocity vector of a cell face per wave directional bin at old time level; $n\theta$: number of wave directional bins.

Process	Criterion
Advection momentum	$\Delta t^{n+1} = \min\|_{\mathrm{cells}} \left(\mathrm{CFL}_{\max} \frac{V^n}{\sum_{faces} Q^n_{out}} \right)$
Advection matter	$\Delta t^{n+1} = \min\|_{\mathrm{cells}} \left(\mathrm{CFL}_{\max} \frac{V^n}{\max(\sum_{faces} Q^n_{out}, \sum_{faces} Q^n_{in})} \right)$
Morphological updating	$\Delta t^{n+1} = \min\|_{\mathrm{cells}} \left(\mathrm{CFL}_{\max} \frac{S_{cell}\,(\Delta z_b)_{\max}}{\alpha_{\mathrm{MF}} \sum_{faces} \sum_{nf} Q^n_{sed}} \right)$
Wave action propagation (Reyns et al., 2023)	$\Delta t^{n+1} = \min\|_{\mathrm{cells}} \left(\mathrm{CFL}_{\max} \frac{S_{cell}}{\sum_{n\theta} \sum_{faces} w {c_g}^n} \right)$

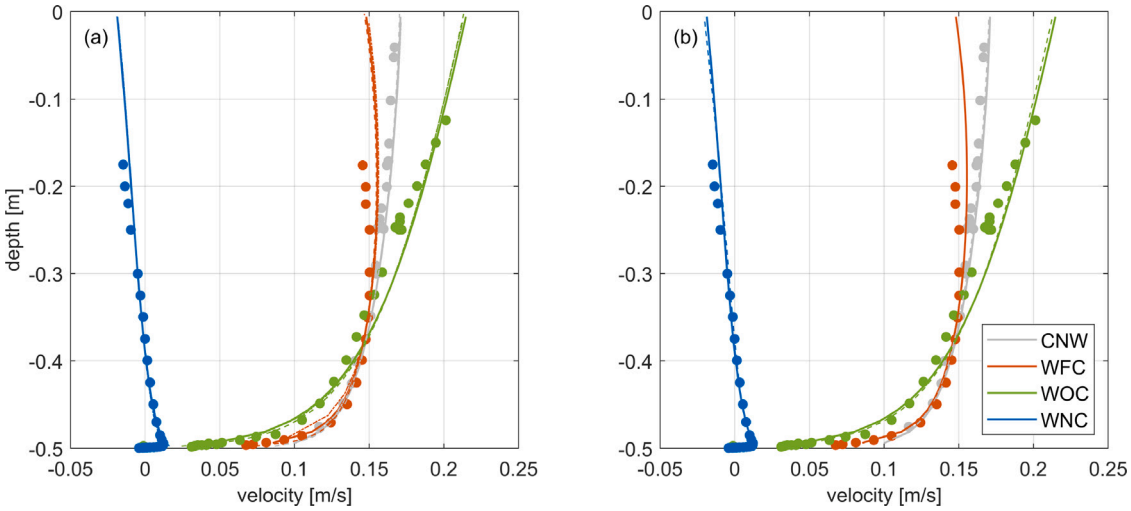

Fig. 1. Klopman (1994) mean horizontal velocities for the flume tests using random waves. Grey: CNW; Red: WFC; Green: WOC; Blue: WNC. (a) Sensitivity to vertical layer distribution. Full lines: 40 layers; Dot-dashed lines: 20 layers; Dashed lines: 100 layers; Dots: measurements; (b) Sensitivity to horizontal grid discretization. Full lines: rectangles; Dashed lines: triangles.

Table 2
Klopman (1994) test conditions. WNC: waves without current; WFC: waves following current; WOC: waves opposing current; CNW: current without waves.

Experiment	H_{rms} [m]	T_p [s]	θ [°N]	**u** [m/s]
WNC	0.12	1.70	270.00	0.00
WFC	0.12	1.70	270.00	0.16
WOC	0.12	1.70	0.00	0.16
CNW	–	–	–	0.16

1). The model is able to reproduce these deviations from the current-only (CNW) profile, however, the vertical shear of the horizontal velocity is underestimated in both cases, and the velocity magnitude is overestimated. In the case of wave propagation without the presence of a current (WNC), the horizontal flow velocity magnitude is underestimated in the upper half of the water column. The depth at which the velocity changes sign, is modelled correctly at 0.12 m above the bed. Near the bed, velocity magnitudes are modulated by the combined effect of non-linear wave–current interaction, which leads to an increase in turbulent shear stress magnitude (Soulsby et al., 1993), and wave-induced streaming (Fredsøe and Deigaard, 1992). Measured near-bed horizontal velocity magnitudes are smaller for both the WOC and WFC cases, relative to the CNW case. This is reproduced correctly by the model. Overall, the model results correspond well with the observations, with low relative bias and scatter index (SCI) values, and a high R^2. Relatively speaking, the WNC case proves to be more challenging than the WOC and WFC cases, as the SCI and the relative bias are higher for the former (Table B.2).

The modelled Eulerian velocities were tested for grid sensitivity, by varying the number of vertical layers, and by discretizing the horizontal plane with rectangles and with triangles (Fig. 1(a,b)). Reducing the number of uniformly distributed vertical layers from 40 to 20 does not have an appreciable effect on the modelled velocity magnitudes for the WNC and WOC cases (Fig. 1(a), blue and green lines). In the case of waves following a current (WFC), reducing the number of uniformly distributed vertical layers distorts the vertical shear in the velocity profile, and reduces the near-bed velocities with up to 7 % to 10 %. This reduction has obvious consequences for the estimation of sediment transport, as both the bedload magnitude, and the reference concentration will relatively decrease compared to the situation with finer vertical layer discretization. Higher up in the water column the velocities increase slightly in the coarser layer models, as mass is conserved. These adverse effects can be mitigated to some degree by the use of a logarithmic vertical layer distribution. The change in horizontal discretization from quadrilaterals to triangles does not lead to important differences in the modelled velocity profiles (Fig. 1(b)).

4.1.2. *Currents under breaking waves*

In the surf zone, spatial gradients in radiation stress induce water level gradients (Svendsen, 1984), and force longshore currents (Garcez Faria et al., 1998). The onshore wave mass flux is compensated by strong Eulerian return flows (Stive and Wind, 1986). Turbulence

Table 3
LSTF case study: test 8E boundary conditions. H_{m0}: significant wave height; T_p: peak period; θ: wave direction; m: cosine power of directional spreading; z_s: water level (Hamilton and Ebersole, 2001).

Parameter	Value
H_{m0} [m]	0.233
T_p [s]	2.5
θ [° from N]	80.0
m [–]	25
z_s [m]	0.0

generated by wave breaking and the generation of rollers, and by wave energy dissipation in the bottom boundary layer, provides additional mixing over the vertical (Justesen et al., 1987). Near the bed, the wave-related Reynolds stresses drive wave onshore directed streaming (Longuet-Higgins, 1953). These processes cause the vertical velocity profile to deviate from a logarithmic solution associated with uniform flow. In this case study, we simulate 3D surf zone circulation under laboratory conditions by comparing to the measurements from the irregular wave case 8E, reported by Hamilton and Ebersole (2001). The test was performed in the Large-scale Sediment Transport Facility (LSTF) of the US Army Corps of Engineers, a wave basin of 50 meter longshore and 30 m cross-shore length. By using an combined system of directional wave boards and pumps, long-crested random waves with a significant wave height of 0.233 m were propagated over a 1:30 linearly sloping bed at an angle of 10° relative to the shore-normal direction. The peak wave period was 2.5 s. The depth at the wave maker was 0.67 m (Table 3).

The numerical model was set up using a domain with a length of 30 m in the longshore direction, and a length of 21 m in the cross-shore direction. We created two cases with differing grids: (1) a 2660 cell grid consisting of rectangles, with a cross-shore resolution of 0.2 m and a longshore resolution of 0.8 m; and (2) a 9837 cell grid consisting of triangles with a spatially uniform average resolution of 0.3 m. Ten vertically uniform σ-layers were used in the vertical domain discretization. The bathymetry was specified in the cell centres. The offshore boundary condition was set to a constant water level of 0.0 m, and a zero water level-gradient signal was imposed on both northern and southern side boundaries. The current-related bed roughness was parametrized using the White-Colebrook formulation (Colebrook and White, 1937), by specifying a roughness height k_s of 1×10^{-3} m. In order to get the correct location for the wave breaker dissipation, we used the internal stationary wave solver combined with a roller model (Nairn et al., 1990; Reyns et al., 2023) to propagate the waves with the characteristics listed in Table 3 towards the beach. The directional resolution was set at 5°. Turbulence was calculated using the k-ϵ model. The model was run for three hours, ensuring a stationary solution. We calibrated the model by tuning the wave breaker dissipation and the roller slope. Wave dissipation was calculated using the Baldock et al. (1998) formulation, with a breaker parameter γ set at 0.8. In order to model the roller energy dissipation, we imposed a constant roller slope β_r of 0.075. All other wave-related parameters were kept to their default values (Section 2.1.1; Table A.1).

The modelled significant wave heights, water levels, the cross-shore and the longshore velocity profiles after 3 h of runtime are shown in Fig. 2. Wave heights decrease throughout the surf zone by depth induced breaking (Fig. 2(a)). The resulting change in wave-related momentum is balanced by a positive water level gradient and a bed shear stress (Fig. 2(b)). In the cross-shore direction, the onshore wave mass flux near the surface is compensated by the undertow (Fig. 2(c)). Wave dissipation by bed friction is an order smaller than dissipation by breaking, so the contribution of streaming to the cross-shore velocity in the surf zone is limited. The alongshore directed component of the wave force vector drives the longshore current, and is balanced by bed shear stress. The model is able to reproduce the wave height profile on the linear slope accurately (R^2 of 0.9, relative bias of 2%, Table B.2). The wave setdown and setup are also modelled correctly. We find a cross-shore distribution of the longshore current that matches the observations relatively well, although the errors are bigger than the ones for wave height and water level. In the cross-shore, the curvature of the velocity profile over the vertical is reproduced reasonably for all stations, but the velocity magnitude is overpredicted on average. Overall, the model produces reasonable results for the hydrodynamics of this test case.

The model was calibrated on the parameter γ in the Baldock et al. (1998) wave breaking estimator, which controls the onset of the wave breaking dissipation; and on the roller slope β_r (Reyns et al., 2023), which controls the magnitude of the wave-related forcing in the momentum balance through the roller energy dissipation. In order to assess the sensitivity of the model to these input parameters, we varied both with 20 %. Comparing the error metrics of the sensitivity runs with the default run shows that the model is insensitive to relatively large changes, in this case (Table B.2). To what extent this holds more generally is to be assessed in the future. Changing the grid discretization from quadrilaterals to triangles has no appreciable effect on the modelled wave heights and velocities. The water levels in very shallow water are lower by ~1 mm, but the reason why is yet unclear (Fig. 2).

4.2. Sediment transport

We validate the sediment transport functionality of our model in three ways. First, we present a case to demonstrate multi-fraction mass conservation by means of sediment settling from a water column out of equilibrium. Secondly, we compare the build-up of an equilibrium sediment concentration profile under current-only uniform flow. Lastly, we simulate sediment concentration profiles in a flume with waves following a current.

4.2.1. Multi-fraction mass conservation

To validate the implementation of sediment settling and resuspension with a closed mass balance, we simulated the transport of three suspended fractions of fines in a water column with a mean depth of 3.75 m. The initial sediment concentrations were set at $0.2\,kg\,m^{-3}$, $0.1\,kg\,m^{-3}$ and $0.05\,kg\,m^{-3}$. The imposed fraction settling velocities are $15.0 \times 10^{-4}\,m\,s^{-1}$, $4.0 \times 10^{-4}\,m\,s^{-1}$ and $0.1 \times 10^{-4}\,m\,s^{-1}$, representing a relatively faster settling, a relatively slower settling, and a quasi-wash load fraction, respectively (Fig. 3). Background molecular viscosity was set to $0\,m^2\,s^{-1}$ to avoid influencing the settling times. All other model parameters were left at their default values (Table A.1).

The 500 m × 500 m domain consists of 382 triangular elements (Fig. 3(a)), and has closed boundaries on all sides. The initial water level was disturbed from rest (Fig. 3(b)), and was allowed to return completely to equilibrium, which took about 2700 s. This water movement caused the sediment on the bed to resuspend during the initial part of the run, and settle through the water column after the water has come to a rest. Sediment transport was calculated using the formulations of Partheniades (1965) and Krone (1962). The run time was set to a duration of 10 h, or 36 000 s. Assuming non-zero sediment concentrations over the entire water column, fraction 1 should settle out completely in 2500 s, fraction 2 in 9375 s, and fraction 3 in 375 000 s after the water level returns to a rest.

Results show that fraction 1 and fraction 2 settle out completely within the duration of the model run, and fraction 3 largely remains in suspension. The remaining mass fraction of the first two sediment fractions after the theoretical settling period has passed is less than 3 % (Fig. 3(c), vertical lines). Over the course of the simulation, the mass balance is closed for all fractions, with a relative error of $O(1 \times 10^{-14})$ (Fig. 3(d)).

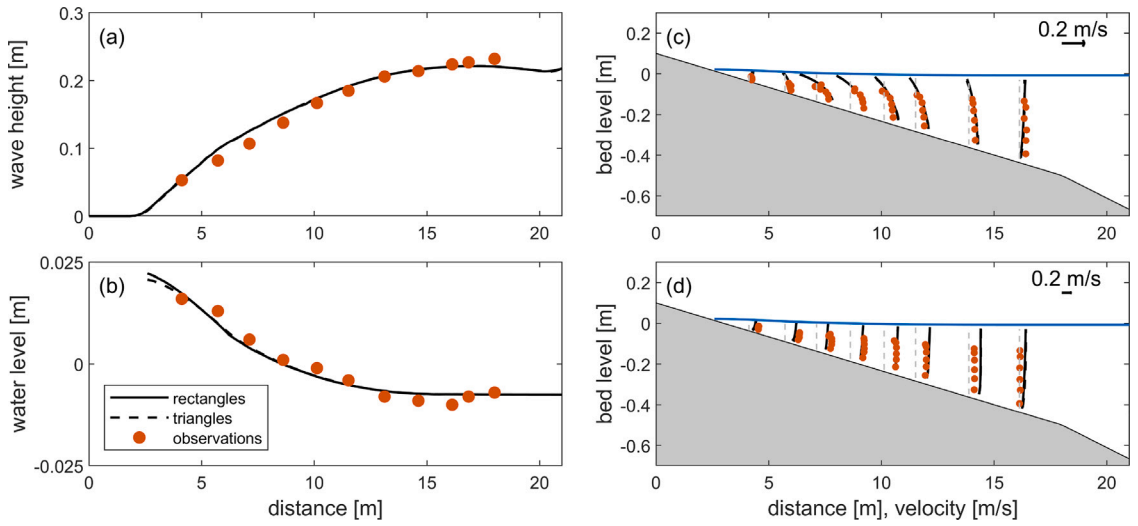

Fig. 2. LSTF case (Hamilton and Ebersole, 2001). Full line: quadrilateral grid; dashed line: triangular grid. (a) Significant wave height; (b) Water level; (c) Cross-shore velocity profiles; (d) Longshore velocity profiles. Red dots: observations; Black lines: model results; Blue line: water level.

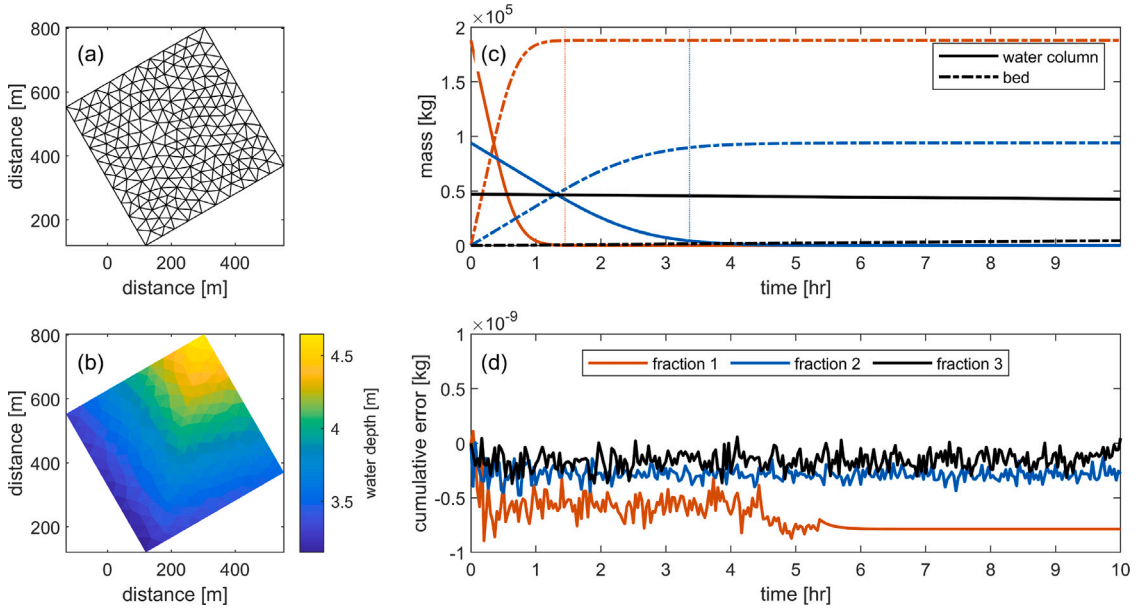

Fig. 3. Multi-fraction mass conservation. (a) Domain discretization; (b) Initial water depth [m]; (c) Sediment mass in the water column (full line), and in the bed (dash-dotted line) over the course of the simulation [kg]. Red: fraction 1; blue: fraction 2; black: fraction 3. The vertical lines indicate the theoretical settling times; (d) Mass error estimates over the course of the simulation [kg].

4.2.2. Sediment concentration build-up under flow-only conditions

Under stationary, uniform flow conditions over an erodible bed, and assuming a parabolic vertical eddy diffusivity distribution, there is a balance between the upward sediment flux due to diffusivity, and the downward flux because of settling. The equilibrium sediment concentration profile has a logarithmic shape, and can be expressed as (van Rijn, 1984):

$$\frac{c}{c_{\text{ref}}} = \left(\frac{h-z}{z}\frac{a}{h-a}\right)^{\frac{w_s}{\beta\kappa u_*}}, \tag{28}$$

where c is the sediment concentration, c_{ref} is the reference sediment concentration at reference height a, h is the water depth, z is the height above the bed, β is the proportion between the sediment vertical diffusivity and the fluid vertical diffusivity, κ is the von Kárman constant, and u_* is the shear velocity. In the rest of this section, we refer to $\frac{w_s}{\beta\kappa u_*}$ as the suspension number λ.

Here, we first test the correct development of sediment concentration profiles in a very long flume. We compare the computed results against the analytical Rouse-Vanoni solution of Eq. (28) at the end of the flume, where equilibrium is reached.

The model domain is 8000 m long, and 30 m wide. The along-flume resolution is 160 m, and the cross-resolution is 10 m, resulting in a total of 150 cells. We imposed a upstream velocity of $2\,\text{m}\,\text{s}^{-1}$, and a downstream water level boundary of 0 m. The flume is 5 m deep, with a bed slope of -3.2×10^{-4}, which represents the equilibrium bed slope when considering a Chézy roughness value of $50\,\sqrt{\text{m}}/\text{s}$. Sediment transport was calculated using the van Rijn (2007a,b,c) formulations. Several model permutations were created by changing the number of vertical logarithmically distributed σ-layers (10, 20 and 50) and the turbulence closure model (algebraic, k-ϵ). Each model was run for a duration of 240 min, and the results were extracted at an observation point located 7500 m downstream from the upstream flume boundary.

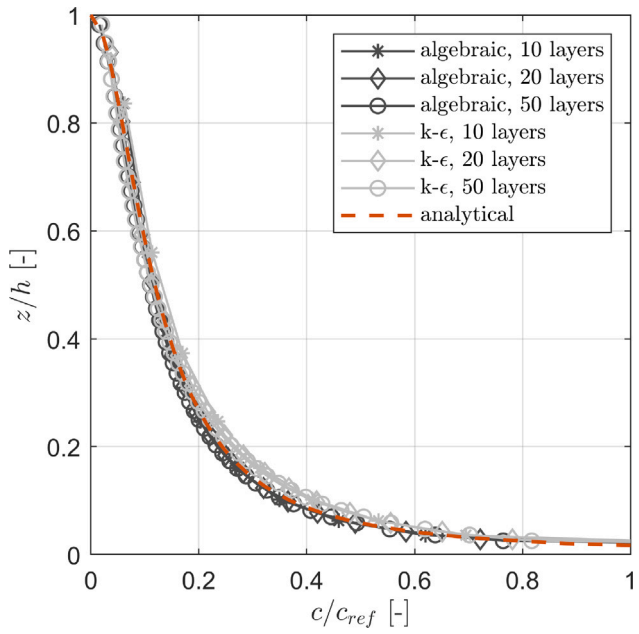

Fig. 4. Rouse-Vanoni dimensionless concentration profiles. Red: analytical solution; Grey: k-ϵ turbulence closure model; Black: algebraic turbulence closure model.

The comparison between the computed equilibrium sediment concentration profiles and the analytical solution (Eq. (28)) is shown in Fig. 4. Apart from deviations near the free water surface as a result of the lack of resolution in the logarithmic layer discretization in the model with 10 layers, the numerical concentration profiles correspond well to the analytical solution. The k-ϵ model overestimates the sediment concentration in the lower quarter of the water column with 6 % to 16 %, and the performance statistics are relatively worse than the ones pertaining to the algebraic models. As expected, results improve with increased vertical resolution (Table B.3).

The build-up of equilibrium sediment concentration profiles along the length of a flume that is initially clear of sediment is shown in Fig. 5. Hjelmfelt and Lenau (1970) developed an analytical solution of the problem, to which we compare our numerical results. The model domain is 120 m long and 1.5 m wide, and is composed of 360 rectangular cells. The cross-flume resolution is 0.5 m, and the resolution along the length of the flume is 1.0 m. The vertical was discretized using 40 σ-layers. A water level gradient was established over the length of the flume to achieve a depth-averaged flow velocity $\overline{U}$ of 1.5 m s^{-1} for a Chézy value of 47 $\sqrt{\text{m}}$/s and a water depth h of 1.0 m. We used an algebraic turbulence model, yielding a parabolic vertical diffusion profile. Morphostatic models were run with three sediment sizes (63.5 µm, 138 µm and 200 µm) that yield the list of suspension numbers λ reported by Hjelmfelt and Lenau (1970) (0.1, 0.3 and 0.5; Fig. 5(b)). The reference height a was set to 0.05 m, following Hjelmfelt and Lenau (1970).

The spatial variation of the dimensionless concentration c/c_{ref} for the d_{50} = 200 µm case is shown in Fig. 5(a). The numerical model reproduces the gradual increase of sediment concentration in the water column with distance along the flume, with an over-prediction of the vertical concentration profile of 2%–4% in the middle of the water column (0.3 to 0.8h). When comparing the effect of different suspension numbers (Fig. 5(b)) on the development of the depth-averaged concentration, we see that in general the resuspension of material is slightly slower in the model relative to the analytical solution. Near the end of the flume, the numerical results converge to the analytical values. The larger the suspension number λ, the longer it takes for the average concentration to reach its equilibrium value. While the solution with $\lambda = 0.5$ approaches equilibrium, the other two solutions do not for the given domain. This reproduced correctly in the numerical results.

Table 4
Concentration build-up under wave–current interaction (Jacobs and Dekker, 2000): boundary conditions. h: depth; d_{50}: median grain size; $H_{sig,\ meas}$: measured significant wave height; $T_{p,meas}$: measured peak period; θ: cartesian wave direction; $\overline{u}_{meas}$: measured depth-averaged velocity; k_s: roughness height.

Test	d_{50} [µm]	h [m]	$H_{sig,\ meas}$ [m]	$T_{p,meas}$ [s]	θ [°]	$\overline{u}_{meas}$ [m s^{-1}]	k_s [m]
m018u	165	0.54	0.19	2.7	0.0	0.0	0.006
m218u	165	0.50	0.15	2.6	0.0	0.19	0.015
m418u	165	0.53	0.15	2.6	0.0	0.33	0.024

4.2.3. Sediment concentration build-up under wave–current interaction

In order to verify the correct implementation of sediment transport under currents and waves, we compare our model results with the measurement data of Jacobs and Dekker (2000), who carried out a number of flume experiments at Delft University of Technology within the framework of the EU SEDMOC project, in order to validate numerical sediment transport models incorporating the effect of currents and waves. The wave–current flume is 45 m long and 0.8 m wide. The water depth in the measurement section during the tests was 0.5 m. Irregular waves were generated in the flume using a piston-type wave board, assuming a JONSWAP spectral shape with a peak enhancement factor of 3.3. For all tests, the wave height and period were 0.18 m and 2.5 s, respectively, resulting in non-breaking wave trains. Currents in the direction of wave propagation were generated by manipulating the discharge using a valve at the upstream end of the flume. Depth-averaged current velocities had magnitudes of 0.0 m s^{-1}, 0.2 m s^{-1} and 0.4 m s^{-1}. The bed of the measuring section of the flume was covered with a 0.1 m thick sand layer. In our test case, we reproduced the runs with a bed composed of sand with a d_{50} of 165 µm (series m018u, m218u and m418u).

The numerical model was set up using a coupling between Delft3D-FM flow solver and SWAN (Booij et al., 1999) every 1800 s, in order to reproduce the effect of the irregular wave field on the transport estimates. The $k-\epsilon$ turbulence closure was used in order to incorporate wave effects in the vertical diffusion profile. The 2.0 m wide and 45.0 m long flow domain was defined on a 1184 cell mixed-element unstructured grid, with an average resolution of 0.25 m. The SWAN domain consists of a curvilinear grid of 9360 cells, with a uniform grid resolution of 0.5 m. The vertical was discretized with 10 or 20 logarithmically distributed σ-layers. The horizontal bed level was set at −0.5 m. Flow boundary conditions were defined using a set of discharge and water level boundaries, resulting in the depth-averaged velocities reported in Jacobs and Dekker (2000) (Table 4). Friction was imposed using the White-Colebrook formulation (Colebrook and White, 1937), with the roughness height taken from the reported ripple dimensions in the flume experiments. The wave conditions were set uniformly on all boundaries of the SWAN model according to the values in Table 4. Sediment transport was calculated using the formulations of van Rijn (2007a,b,c). Calibration settings were left at their defaults (Table A.1), and the model was run for 3600 s.

Comparison of the numerical results with the observations show reasonably good agreement (Fig. 6). As in the Klopman WFC test (Section 4.1.1), the velocity near the bed is reduced, and the presence of waves bends back the profile shape. Higher discharges lead to more sediment resuspension, higher in the water column (Fig. 6(b,c)). The velocities are predicted more reliably than the concentrations, which are under-predicted by a little less than 10 % overall. Both velocity and concentration are predicted better when using 20 layers, notably in the upper part of the water column, as a result of the increased resolution (Table B.3).

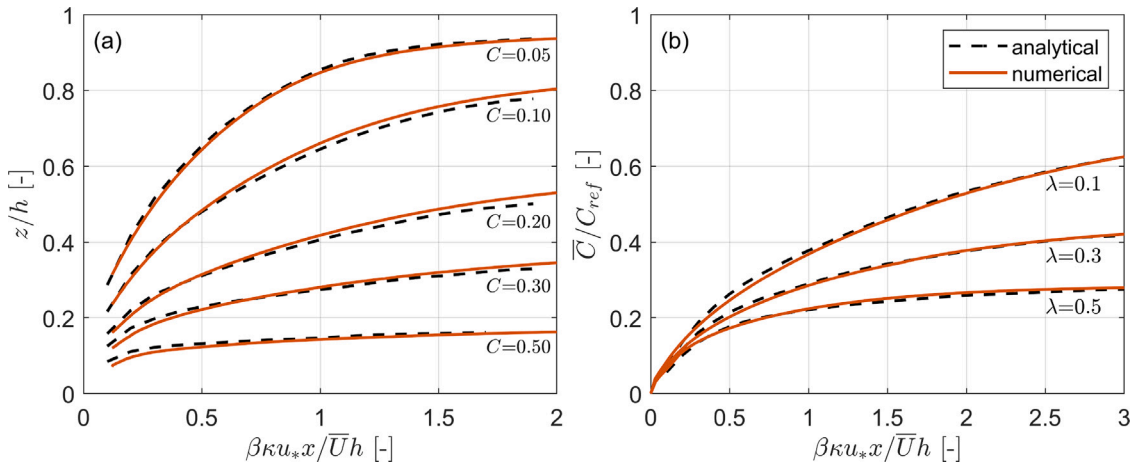

Fig. 5. Sediment concentration build-up along a flume (Hjelmfelt and Lenau, 1970). (a) Dimensionless concentration C as a function of dimensionless distance along the flume $\beta\kappa u_* x/\overline{U}h$ for d_{50} of 200 μm, reference height a of 0.05 m, and a suspension number λ equal to 0.5. Black: analytical solution; Red: numerical result. (b) Dimensionless depth-averaged concentration as a function of dimensionless distance along the flume for different suspension numbers λ. Black: analytical solution; Red: numerical result.

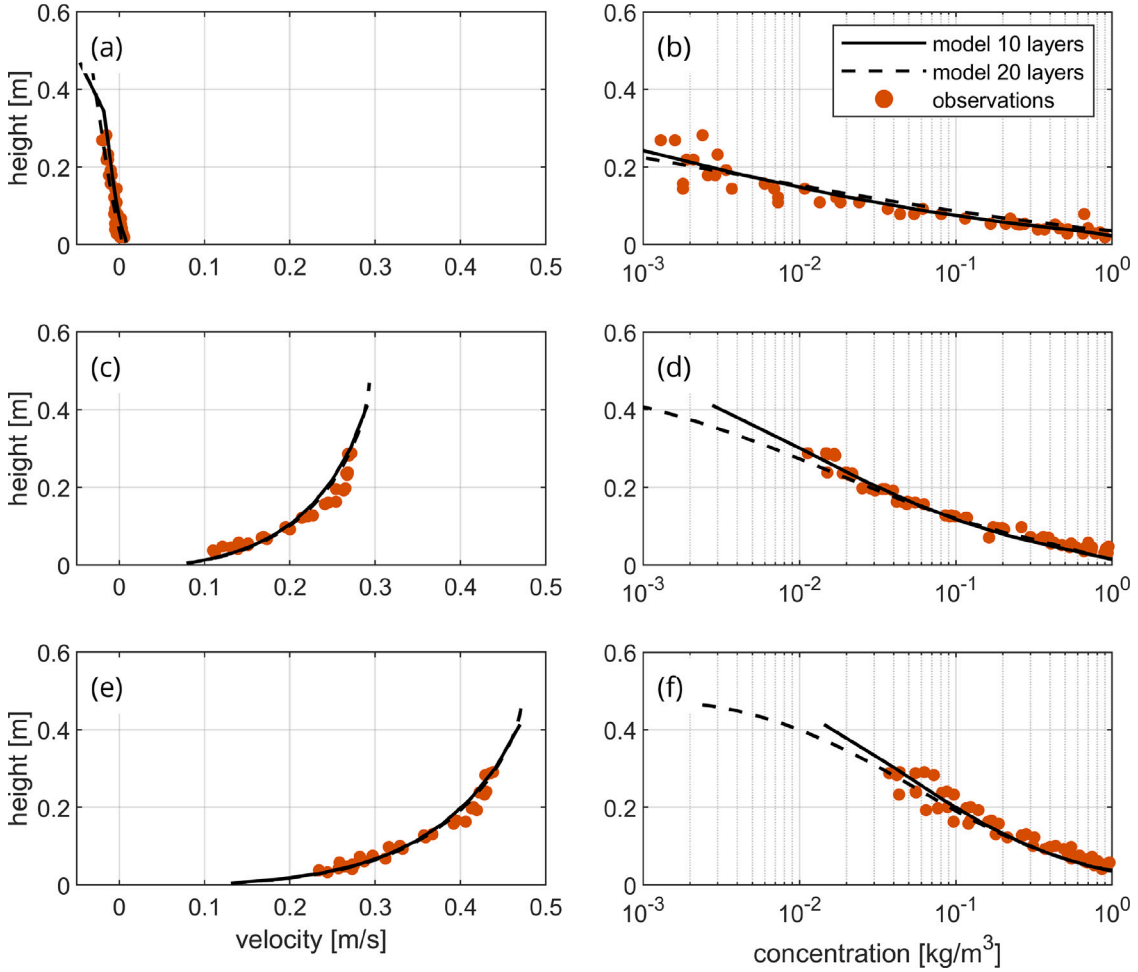

Fig. 6. Sediment concentration build-up under wave–current interaction (Jacobs and Dekker, 2000). Significant wave height H_s: 0.18 m; peak wave period T_p: 2.5 s; water depth: 0.5 m; depth-averaged velocity $\bar{u}$: (a,b) 0.0 m s^{-1}; (c,d) 0.2 m s^{-1}; (e,f) 0.4 m s^{-1}.

4.3. Morphology

In this section, we present six verification cases that demonstrate the ability of the model to produce reliable morphodynamic results. The first case simulates the development of a constant slope under uniform flow forcing in a numerical flume. The migrating trench case (van Rijn, 1980) aims to reproduce morphological changes observed in a flume under unidirectional flow conditions. Breaching of a sand body

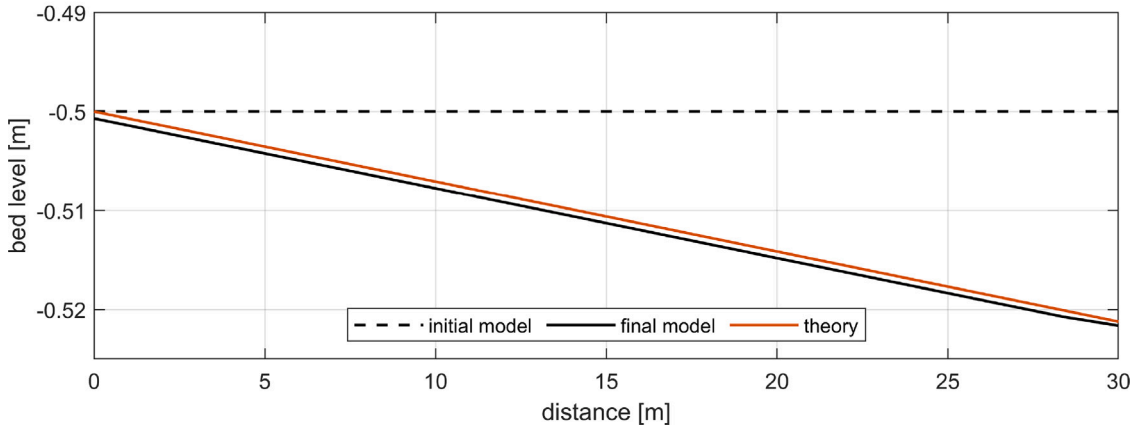

Fig. 7. Development to an equilibrium slope. Red: theoretical bed level; Black: modelled bed level at start (dashed) and end (full line).

under field conditions with sediment slumping is modelled in the Zwin case (Visser et al., 1995). The model features implemented to simulate extreme storm impacts are demonstrated in the ECL case. Finally, we present a model that studies the circulation and morphodynamics of sandy beaches protected by emergent structures.

4.3.1. Equilibrium slope

A first basic test to check the implementation of the bed update functionality is the development towards an equilibrium bed slope under uniform stationary flow conditions. Under uniform, stationary flow, there is a balance between the gravitational and the frictional forces:

$$\frac{\partial \eta}{\partial x} = \frac{|\boldsymbol{u}| \cdot \overline{u}}{h\, C^2} \tag{29}$$

Under these conditions, horizontal flow accelerations are $0.0\,\mathrm{m^2\,s^{-1}}$, sediment transport gradients are $0.0\,\mathrm{kg\,s^{-1}\,m^{-2}}$, and the bed is parallel to the water surface. In this test, we considered a 2DH domain of 30 m long, 0.5 m wide, and with an initial uniform water depth h of 0.5 m. The initial bed was horizontal at a level of −0.5 m. The grid resolution was set at 0.25 m in the direction along the flume, and at 0.15 m across the width of the flume, for a total of 484 cells. We imposed a incoming total discharge of $0.25\,\mathrm{m^3\,s^{-1}}$ at the upstream end, and a water level η of 0.0 m at the downstream end. The bed roughness was defined using a Chézy parameter C equal to $50.0\,\sqrt{\mathrm{m}}/\mathrm{s}$, which should result in a water level slope and a bed slope of 8×10^{-4}. The morphological acceleration factor was set to 20. All other settings were left at their defaults (Table A.1). The model was run for 15 h hydrodynamic hours, and the final bed level was plotted in Fig. 7. The results show that the equilibrium slope is reproduced by the model. At the downstream end, the slope deviates from the analytical solution as a result of the zero-gradient Neumann condition for bed levels we impose at outflow boundaries.

4.3.2. Van Rijn (1980) migrating trench test

van Rijn (1980) carried out measurements of fluid velocity, sediment concentrations and morphological development of a 0.175 m deep trench dug in the sandy bed of a 30 m long, 0.5 m wide, 0.7 m deep flume. Trench slopes for tests were set at 1:3, 1:7 and 1:10. The 0.2 m thick sandy bed had a d_{50} of 160 μm. The depth-averaged flow velocity during the experiment was set at $0.51\,\mathrm{m\,s^{-1}}$, at an upstream water depth of 0.39 m. Sediment was fed to the flume at a rate of $0.04\,\mathrm{kg\,s^{-1}\,m^{-1}}$, which corresponds to equilibrium transport conditions. After 15 h, the bed level was recorded to register the migration and amount of infilling in the trench (Fig. 8(a)).

Here, we modelled the case with the trench slope equal to 1:3, for which van Rijn (1984) reports the measurement data. The model domain is 30 m long, 0.5 m wide, and has 995 quadrilateral elements. The horizontal grid resolution is 0.15 m along the flume and 0.1 m across. The vertical was discretized using 10 logarithmically distributed σ-layers, in order to better capture the near bed gradients in flow velocity and sediment concentrations. Upstream, a discharge boundary with a constant value of $0.0975\,\mathrm{m^3\,s^{-1}}$ was imposed. On the downstream end, we used a water level boundary with a value of 0.41 m. The bed roughness was set using the White-Colebrook formula, with a k_s value of 0.03 m, based on the observed current ripples in the flume. Turbulence was modelled using the algebraic model. The d_{50} sediment diameter was specified as 160 μm. The model was run for 40 min hydrodynamic time, in a version incorporating bed level changes, as well as in a version without. In the version with bed updates, the morphological start time was set at 20 min after the start time of the model to allow for the establishment of stationary transport conditions before bed changes take place. A morphological acceleration factor of 45 was applied to arrive at a total of 15 h of morphological change. Proportionality factors κ_{bed} and κ_{sus} for bed and suspended load were set to 0.85. All other model parameters were left at their default values (Table A.1).

The resulting bed level changes, velocity and sediment concentration profiles are shown in Fig. 8. The trench infilling is modelled with a volume error of 0.7 %, and at the correct infilling rate (Fig. 8(a)). The sediment concentration profiles along the flume reflect the flow pattern of deceleration and acceleration across the trench, including the near-bed flow reversal near station *Obs4* (Fig. 8(b)). Flow velocity and sediment concentrations are underestimated with 8.0 % and 4.0 %, respectively (Table B.3). Upstream of the trench, the equilibrium transport conditions are reproduced correctly (station *Obs1*). In stations *Obs4* and *Obs6*, in the area with large horizontal velocity gradients and recirculation, the model reproduces the rapid decrease in concentration. The resuspension of sediment in the accelerating flow in stations *Obs7* and *Obs8* is somewhat underestimated.

4.3.3. Zwin breach experiment (Visser et al., 1995)

Avalanching (Section 2.2) allows for the calving off of steep exposed faces of erosion cliffs, under conditions like wave attack on a dune front (Roelvink et al., 2009), or during the growth phase of a breach in a sand body (Bokuniewicz et al., 2011). Growth of a breach in a sand barrier is simulated in this test case, where we reproduce the measurements in the Zwin inlet on the border between Belgium and the Netherlands, as reported by Visser et al. (1995) . A $5100\,\mathrm{m^3}$ artificial bar made of 300 μm sand, with a top level of 3.3 m above NAP (Dutch vertical reference level, approximately MSL) was constructed over the inlet. At the start of the experiment, just before high tide (+2.65 m NAP), a 2.0 m wide channel at +2.5 m NAP, with 1:1 side slopes was

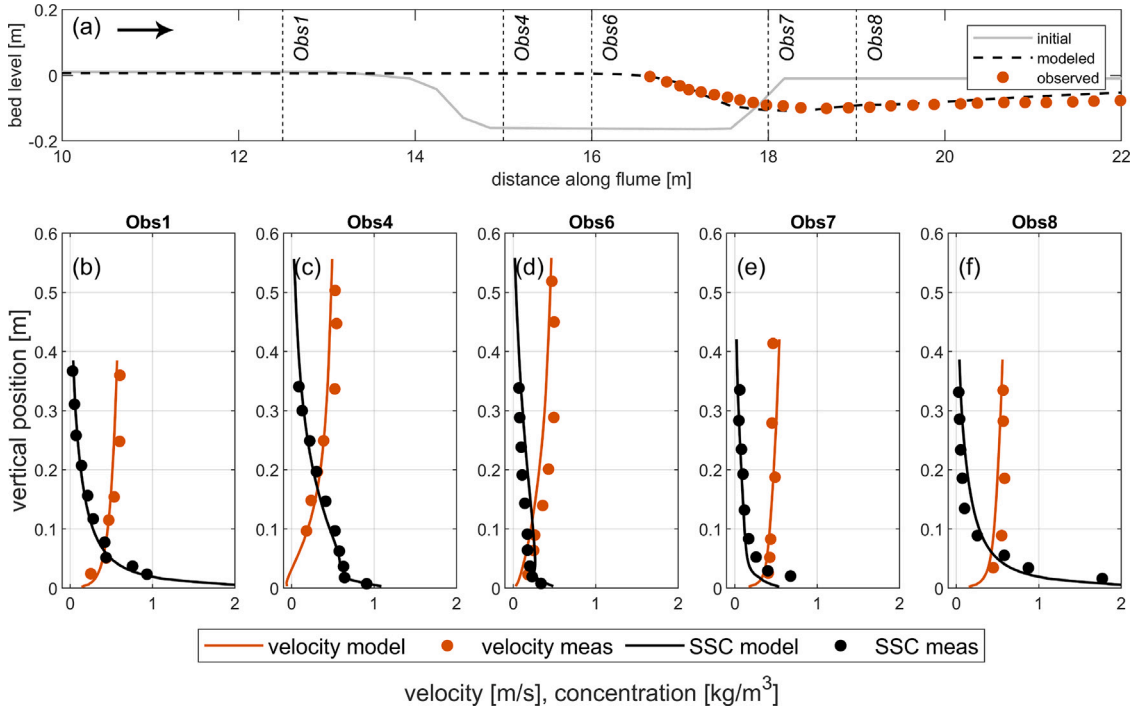

Fig. 8. van Rijn (1980) trench migration case. (a) Bed level at start (grey); modelled (black dashed) and measured (red dots) final bed level of morphodynamic experiment. Black arrow indicates direction of inflow. (b–f) Measured (dots) and modelled (full line) flow velocity (red) and sediment concentration (black) at stations after 10 min hydrodynamic time, without bed level update.

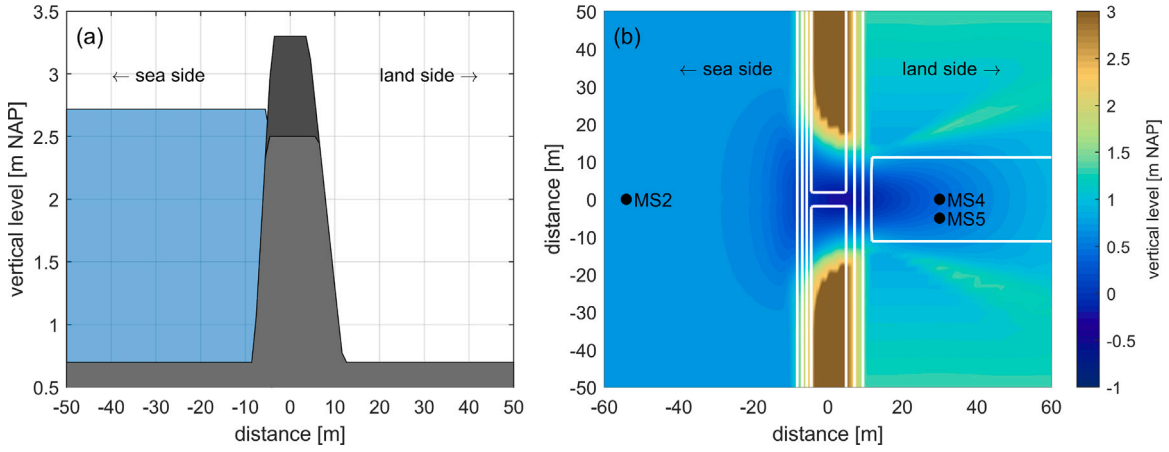

Fig. 9. Zwin breach experiment (Visser et al., 1995). (a) Initial sand bar configuration and water level. Dark grey: supratidal level of sand bar; light grey: sand bar level at initial breach level; blue: tidal water level at breach initiation. (b) Final modelled bed level. White: contours of initial bed level at 0.75 m intervals. For reference, the inner contour of the sand body is at +3.0 m NAP. Black dots: locations of measurement stations from Visser et al. (1995).

mechanically opened to initiate the breaching process. During the next hour, until the water levels on either side of the breach levelled out and flow through the breach stopped, water levels, velocities, scour hole depth and breach width were monitored in a number of fixed stations (Visser et al. (1995), Fig. 9).

The 2DH morphodynamic model schematizes the Visser et al. (1995) field setup, incorporating a sand body with prototype dimensions in a rectangular domain of 2800 m by 1000 m. The grid resolution varied between 0.5 m and 50 m according to expected bed level change magnitude, for a total of 13 736 cells. The bed levels were adopted from Roelvink et al. (2009). On the seaward side, the initial water level was set at the measured tidal level at the beginning of the experiment, and the landward end is dry (Fig. 9(a)). The model was forced by the measured tidal signal on the seaward side, and the boundary on the landward side was closed. Waves were not included. The bed roughness was specified using a Manning's coefficient of 0.023. Sediment transport was calculated with a simple bedload formula (Meyer-Peter and Müller, 1948), calibrated to reproduce the breach growth time series (Fig. 10(a)), in line with e.g. Visser (1995). Optimal results were obtained with a proportionality factor κ_{bed} of 10.0 for the sediment grain size of 300 μm present in the bar (Visser et al., 1996). To activate the avalanching mechanism, the critical bed slope for cells with less

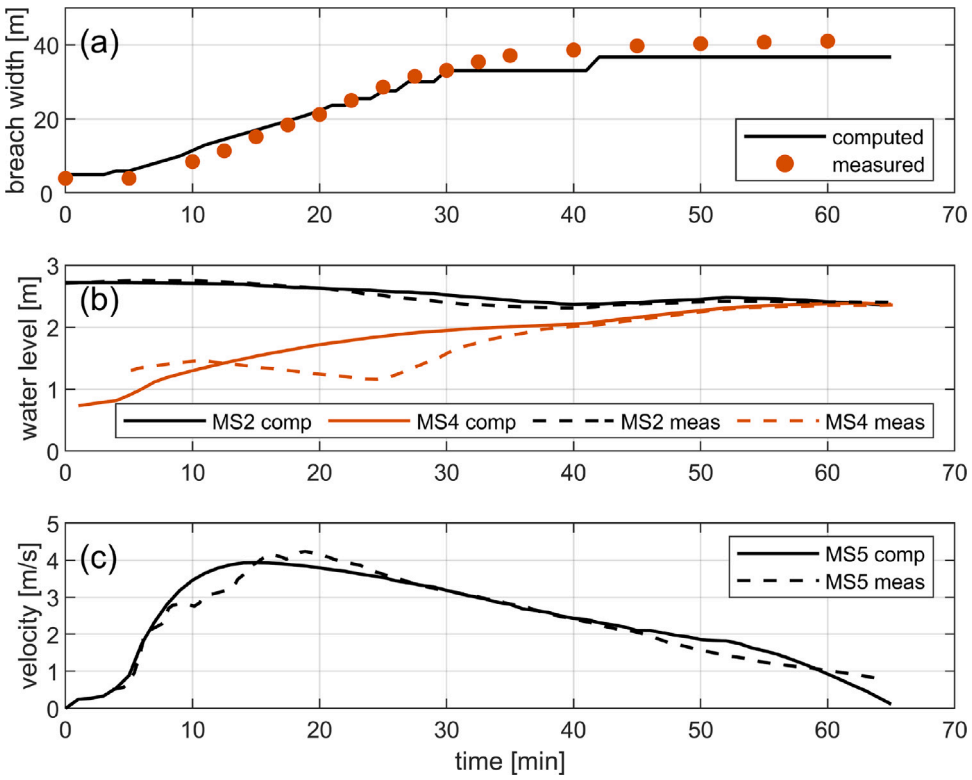

Fig. 10. Zwin breach experiment (Visser et al., 1995) base run results. (a) Measured (dots) and modelled (line) breach width development. (b) Measured (dashed) and modelled (full line) water levels in station MS2 (black) and MS4 (red). For station positions, see Fig. 9. (c) Measured (dashed) and modelled (full line) flow velocity signal in station MS5.

than 0.1 m of water depth was set to $\tan(45°)$. All other parameters were left at their default values (Table A.1).

The model results of the base run were compared with data derived from the measurement setup deployed around the breach Fig. 10. The breach growth process follows the conceptual model described by Visser (1999), with regressive and vertical erosion without width changes in the first 5 min, and successive lateral widening. In our results, the initial phase of breach widening starts too early compared to the field data, and the widening rate is too slow compared to the measurements. Over the entire run, the breach width error is around 15 %, and the final width is underpredicted by 10 % (Fig. 10(a)). The water levels and the velocities have an error of 25.0 to 30.0 %, which is mainly related to the large deviations from the measured signal in MS4 and MS5 in the first 30 minutes of the test (Fig. 10(b,c)). Visser et al. (1996) indicate that data in MS4 before t=35 min and in MS5 before t=30 min should be treated with caution. If we remove these data and recalculate the error statistics, the error reduces to less than 15 % for both velocity and water level. Given the schematized nature of the numerical model, we deem these results to be satisfactory. We ran a sensitivity analysis by changing the transport rates by 10 % to influence the vertical breach growth, by lowering the critical slope for dry cells to induce faster breach growth, and by recalibrating the model using the sediment transport relations of van Rijn (1984), as was done by Visser (1995). None of these changes had a very large effect on the modelled breach characteristics and the associated errors, demonstrating the robustness of the model results (Table B.3).

4.3.4. 2016 East Coast Low, Sydney, Australia

One of the main applications of modern process-based coastal morphodynamic area models is the assessment of the hazards and impacts related to extreme storm events. Here, we test the ability of our model to hindcast the unusually large erosion hazard resulting from the East Coast Low (ECL) that occurred in the period of June 4th–7th 2016 along the south-east coast of Australia (Fig. 11(c–f)). The storm conditions were anomalous because of the north-easterly incident wave direction, severely impacting beaches along the New South Wales coastline (Mortlock et al., 2017). Our domain of interest is the Narrabeen - Collaroy embayment, which experienced significant erosion during the event. Bed levels were measured over part of the bay by lidar and echosounder (Beuzen et al., 2019; Harley et al., 2017) before and after the storm, and serve as validation data.

Model setup. The model domain covers the Narrabeen-Collaroy embayment, Turimetta Beach and Warriewood Beach. The Narrabeen lagoon was included between the inlet mouth and Ocean Street Bridge. The offshore boundary was established along the −40 m bed level contour. The grid has 160 058 cells, and the resolution varies between 20 m offshore and 1 m on the supratidal beach and dunes (Fig. 11(a,b)). The bed levels relative to Australian Height Datum (AHD) were derived from a number of sources. The pre-storm (1st June 2016) measured topo-bathymetry was used in the Narrabeen-Collaroy bay where available, and was complemented with data of NSW DCCEEW (2019) and Nsw DPI (2019). We assumed that the pre-storm bathymetry did not fundamentally differ from the prevailing bathymetry on June 4th. Spatially varying sediment availability was mapped using the benthic habitat classification of NSW DCCEEW (2022). Based on our knowledge of the study area, reef areas were given a sediment thickness of 0.5 m, and subtidal sandy areas and beaches, a thickness of 20 m. In locations where the post-storm orthophotos showed bedrock or protective structures being laid bare by the storm event, we set the sediment thickness to the eroded layer thickness derived from the post-storm topographic survey data. Hardened surfaces (streets, parking lots, building footprints) were extracted from the OpenStreetMap database (Open Street Mapc ontributors, 2022), and imposed as unerodable layers. Detailed spatial repartition of grain sizes was not publicly available, therefore we used a single fraction, and we set the median sediment grain size to a fixed

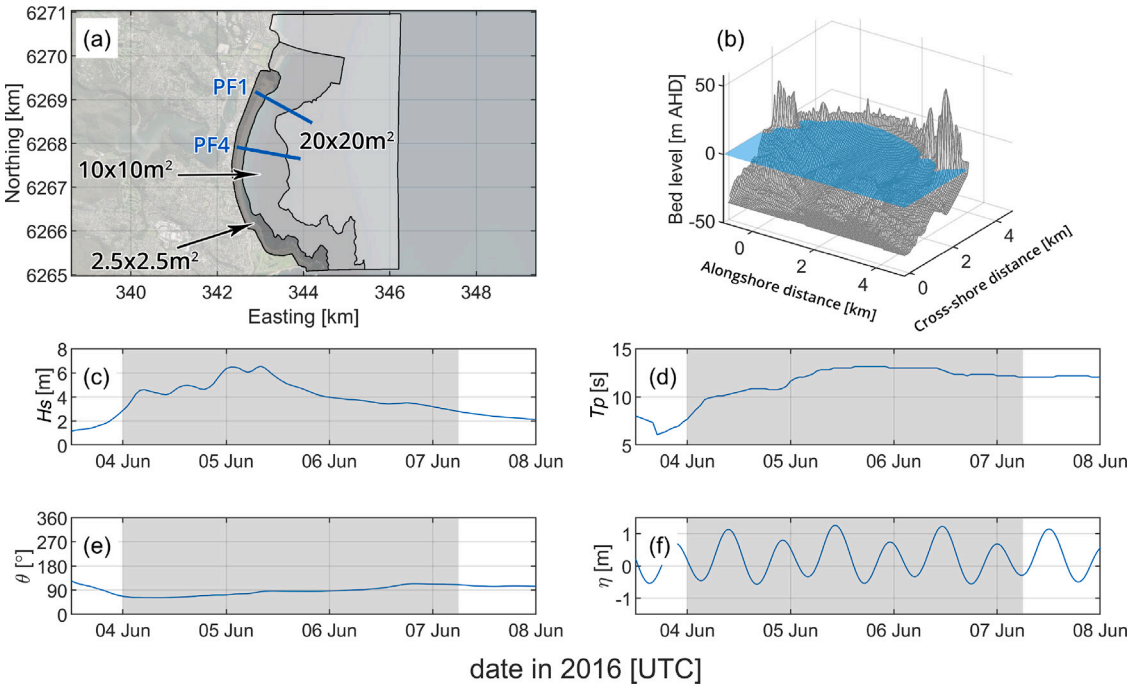

Fig. 11. 2016 ECL model domain and boundary conditions. (a) Grid extent and resolution. In the supratidal area, the resolution is further increased to ~1 m. The location of profiles PF1 and PF4 are indicated in blue. (b) Initial bathymetry. (c-f) Significant wave height H_s; peak wave period T_p; wave direction θ; and surge level η. The simulated period is indicated in grey.

value of 300 µm (Bracs, 2016; Turner et al., 2016). The Manning bed roughness was set to 0.024 in non-vegetated areas. To simulate the influence of vegetation on the erodibility of dunes, we implemented the dynamic vegetation roughness mechanism of van der Lugt et al. (2019). Vegetation patches were identified from the pre-storm Google Earth satellite imagery (Google, 2022), and were assigned a Manning parameter value of 0.045. The root depth of local foredune vegetation was set conservatively at 0.5 m (Bryant et al., 2017).

The model was forced by water level and wave energy boundary conditions at the wave group timescale (surfbeat mode, Reyns et al., 2023), effectively incorporating the contribution of infragravity waves to the storm-induced hydro-morphodynamics. Time series of the total offshore water level signal, including tides and storm surge, were derived by low-pass filtering the measured signal from the nearby Fort Denison tidal station data (MHL (2022a), Fig. 11(f)). On the Narrabeen lagoon side, water levels measured at Ocean Street Bridge (MHL, 2022b) were imposed on the model at the inflow location. The northern and southern boundaries were forced with a zero water level-gradient signal. Wave boundary conditions were derived from the modelled bulk wave parameters from the nearest offshore grid point in the CAWCR wave hindcast database (Durrant et al., 2019). Maximum incident waves from the east reached heights up to 6.4 m and periods of 13 s to 14 s in the morning of June 5th, coinciding with spring flood tide during the second half of the storm peak. The model was run in single-direction surfbeat mode (Reyns et al., 2023) for 15.6 h with a morphological acceleration factor of 5, covering the period between the onset of the event and the post-storm bathymetric survey. Wave directions were discretized at a resolution of 2.5°. We applied the van Thiel/van Rijn sediment transport formulations (Section 2.2.3), with wave non-linearity factor *facua* calibrated to 0.4 on the profile evolution of PF1, and validated on PF4 (for profile locations, see Fig. 11(a)). Avalanching was switched on with a critical dry slope of 1.0, and the swash slope to nudge to was set at 0.25, which corresponds to the average observed post-storm intertidal beach slope. The 2DH model was run in parallel mode using a total of 16 domains.

Results. The observed morphological impact of the 2016 ECL storm event was severe dune scarping and erosion of the upper beach, with deposition of the sediment in two linear offshore bars (Fig. 12(f)). One bar formed offshore of the beach fronting South Creek (in the zone from 500 m to 1000 m, Fig. 13(a)), and the second one covered most of the surf zone in the southern half of the embayment (1400 m to 3000 m). The distribution of the erosion volumes of the dune front and the upper beach was quite uniform over the length of the domain (Fig. 13(a)). Along the southern end of the bay, cross-shore erosion was spatially constrained by the presence of infrastructure.

Fig. 12 shows the erosion/sedimentation patterns as a function of time throughout the storm. The final model results show a morphological development that is in reasonable agreement with the observations (skill score of 0.59, bias of −0.07 m for the base case, Table B.4, Fig. 12(e,f)). In the period before the peak in wave heights (5th June, 01:00 AM), the intertidal beach and the dunes along the bay erode in a rather spatially uniform pattern, and the eroded sand is deposited in water depths of 4 m to 5 m in the form of a linear bar (Fig. 12(b)). A large rip current develops at the Collaroy end of the bay and persists throughout the simulation, with the velocity magnitude varying according to the prevailing wave height (not shown). A similar flow pattern was presented by Mortlock et al. (2017). The spatial gradients in longshore transport magnitude going from north to south leads to erosion at P1100 and deposition at P2000 (Fig. 12(f)). In the southern part of the bay (P2800), transport magnitudes are relatively low and directed northward, promoting sediment convergence near the bar offshore of Collaroy. The longshore transport magnitude decreases strongly in the evening of June 5th, concurrent with a drop in wave height under 4.0 m. Moreover, the incident wave direction veers more to the east to south-east, and over the next two days, the eroded sand volumes

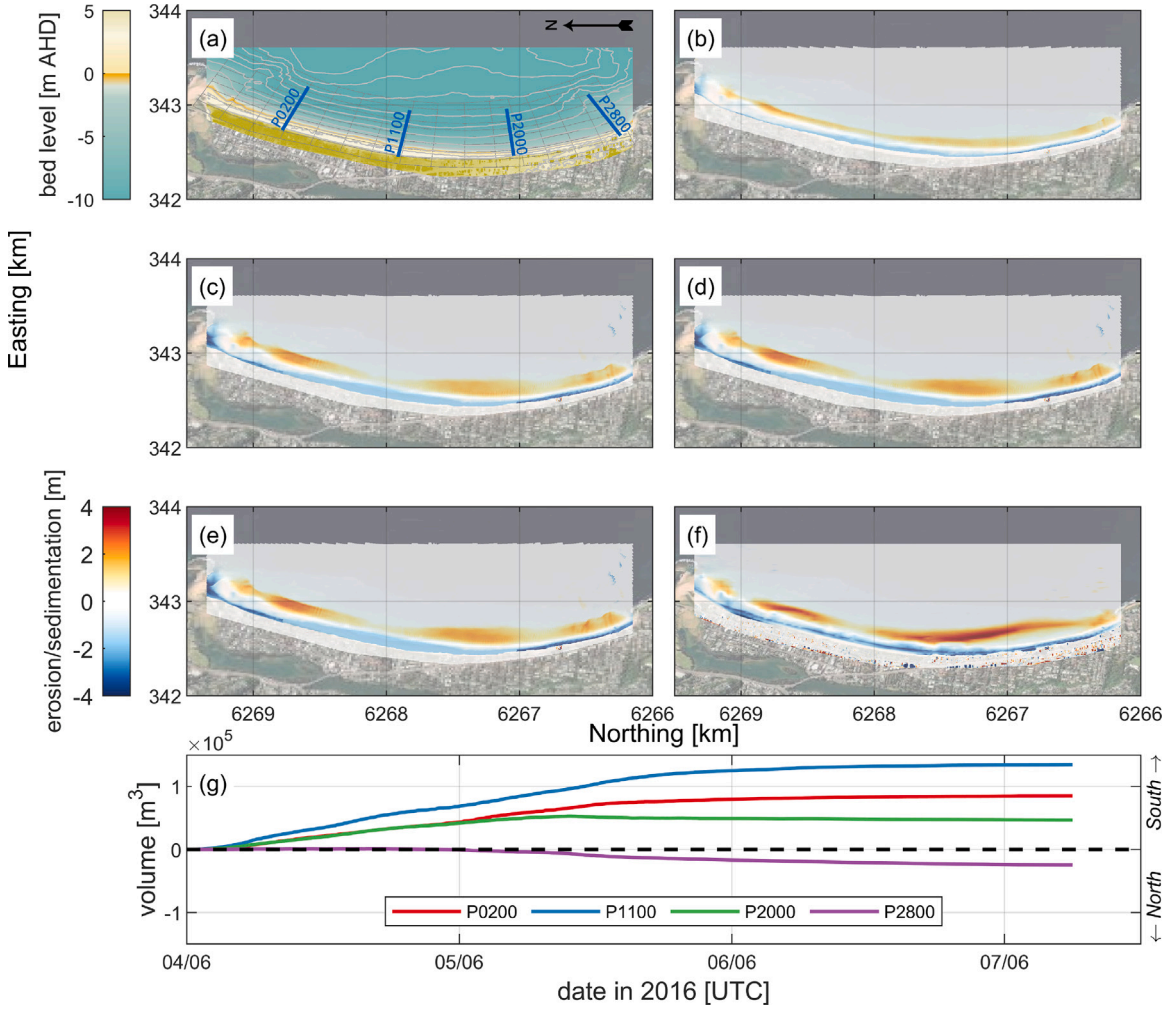

Fig. 12. Erosion/sedimentation patterns ECL 2016 case. (a) Initial bathymetry; Grey grid defines the control volumes for the bed level change comparison. Blue profiles correspond to P0200, P1100, P2000 and P2800, going from north (left) to south (right). (b) Modelled erosion/sedimentation patterns on 5 Jun 2016 00:00; (c) 6 Jun 2016 00:00; (d) 7 Jun 2016 00:00; (e) 7 Jun 2016 06:00. (f) Final observed erosion/sedimentation. (g) Cumulative sediment transport through 4 transects defined in (a). Positive values correspond to transport to the south.

are further reworked into the two bars that are observed in the post-storm bathymetry, although morphological activity is much reduced compared to the first day of the event (Fig. 12(c–e)).

The model reproduces the general pattern of sediment volume redistribution within the bay, where the central part of the embayment loses sediment volume, and the northern and southern ends see an overall increase in available sand (Fig. 13(a)). A total volume of about 35 000 m^3 is imported in the Narrabeen-Collaroy embayment over the course of the storm event from the beaches to the north (90%) and south (10%). The main discrepancies between model results and observations are the overprediction of the subtidal volume in the northern part of the study area, and an underprediction of the subtidal sediment volume in the central part of the bay, and of the sediment volume stored in the southern surf zone bar. The difference between the nett volume change over the storm predicted by the model and that derived from observations is ~90 000 m^3, which is in the order of the measurement uncertainty (taken as 0.03 m, Mortlock et al. (2017)) multiplied by the control volume area.

In this test case, we used bulk wave data originating from the CAWCR dataset (Durrant et al., 2019), as available wave buoy records during the storm feature important data gaps. In order to assess the variability of the modelled morphology as a function of the uncertainty associated with the wave boundary conditions, additional model runs were undertaken where the wave height, the wave period and the wave direction were varied (Table B.4). Results demonstrate that changing the incident wave direction by 10° in either direction has negligible effects on the skill of the morphological prediction. However, lowering the wave period or the wave height with 20 % improves the skill to 0.62 and 0.68, respectively. This improvement was due to a reduction in the amplitude of the volume changes along the embayment. The non-linearity parameter *facua* was used to calibrate the cross-shore profile behaviour in the intertidal zone. Varying this parameter with 20 % has minimal effect on the overall skill of the model (Table B.4).

4.3.5. Offshore breakwaters

Offshore breakwaters are a widely used engineering intervention to control sedimentation processes in microtidal areas characterized by small tidal current velocities, and when the wave climate is low to moderately energetic. They induce substantial wave energy reduction in their lee side. These spatial gradients in wave energy fluxes create recirculation cells (Mory and Hamm, 1997), which transport sediment into the zone directly behind the structures. The morphological result

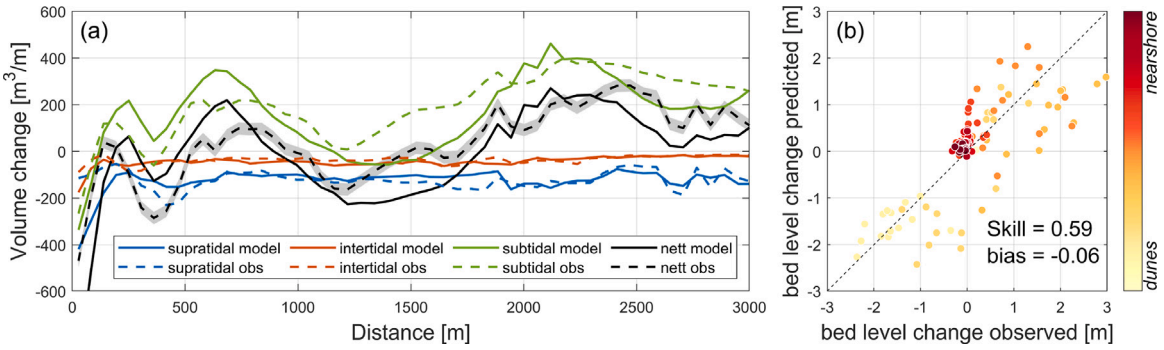

Fig. 13. Erosion/sedimentation volumes ECL 2016 case. (a) Volume changes in supratidal (blue), intertidal (red) and subtidal zones (green) along the Narrabeen–Collaroy embayment. Full line: modelled; dashed line: measured. Grey band indicates the measurement uncertainty for the bathymetry. (b) Comparison of average bed level changes within volume control boxes (Fig. 12(a)). Colours indicate relative cross-shore position of data points. High tide level was taken as 0.93 m AHD, and low tide level as −0.60 m AHD.

is the formation of salients or tombolos, depending on the geometry of the breakwater field (Hsu and Silvester, 1990), and the characteristics of the dominant wave forcing (e.g. Rosati et al. (1992)). An overview of empirical criteria predicting shoreline response is given in Reeve et al. (2018).

In this test case we aim to reproduce the equilibrium morphology in the lee of a field of emergent breakwaters. To this end, we simulated the development of a number of salients in the lee of a field of 3 shore-parallel breakwaters. The geometry of the model setup and the physical forcing of the model are based on those of a detached breakwater field west of Alexandria, Egypt. This field of breakwaters was constructed 200 m offshore in the period between 2001 and 2005. The length of each breakwater is 100 m, and they are spaced 50 m apart. The structures were placed in a water depth of around 4 m to 5 m, and have a crest level at 1 m above MSL (Iskander et al., 2007). Based on Pope and Dean (1987), the expected morphological response is the buildup of salients, which is reflected in the current satellite imagery of the study area (Fig. 15(c)). Measurements reported in Iskander et al. (2007) show that over their monitoring period of 4 years, the shoreline in the lee of the breakwaters indeed took the shape of a number of salients, with an average shoreline progradation of 40 m.

As detailed public bathymetry data over the period 2001 to 2003 are lacking, we set up a schematized coupled flow-wave model with the characteristics of the Al Nakheel detached breakwater field. The unstructured flow grid spans a distance of 560 m alongshore and 360 m cross-shore, with a resolution increasing from 10 m to 5 m going from offshore to onshore. In order to accommodate diffraction, the flow model was coupled to the SWAN model, with a coupling interval of 1200 s. The wave model domain extends laterally beyond the flow domain to accommodate boundary disturbances, and has a resolution similar to the flow grid where they overlap. The final grid sizes were 8355 elements for the flow model and 21 000 cells for the wave model. The vertical dimension was discretized using 10 σ-layers with logarithmic refinements near the bed and the surface. Turbulence was modelled using the $k-\epsilon$ model, in order to incorporate the influence of the presence of waves on the vertical viscosity. The initial bathymetry was defined using a Dean-type equilibrium profile that was scaled by using the local mean sediment grain size of 300 μm (Iskander et al., 2007). The model was forced using wave conditions only, as the tide range in this area is considered to be negligible (Hendy et al., 2021). The water level was set at mean sea level. The lateral boundaries of the flow domain were defined using zero water level gradients. Wave boundary condition data were taken for the period 2000 to 2023 from the ERA5 grid point (Hersbach et al., 2020) closest to Alexandria, and schematized into 9 conditions using the wave energy flux method (Lesser, 2009). These forcing conditions were combined in a parallel online (Roelvink, 2006) morphodynamic run, where conditions are weighted using their frequency of occurrence. The nett wave energy flux is towards the north in our model. The model time was set to simulate 1 year of morphological change. Wave diffraction was switched on. At the location of the breakwaters, the sediment availability was set to zero. Elsewhere, a layer of 10 m of sediment was available. Sediment transport fields were calculated using the van Rijn (2007a,b,c) formulations. All other model parameters were left at their defaults (Table A.1). The model was partitioned in three domains, and run using MPI.

Results show a complex flow pattern around the breakwater field as a function of the direction of the incoming wave field. Typical flow and sediment transport conditions are shown in Fig. 14. Incident waves break on the emergent breakwaters, and diffract around the tips of the structures. At the upstream end, the undisturbed longshore current field driven by wave forces extends into the lee side of the structures, and advects sediment along the shoreline behind the breakwaters (Fig. 14(a,b)). At the downdrift end of the breakwater field, a circulation cell is generated that advects sediment towards the lee side of the last structure. In the gaps between the structures, the sign of the vorticity field and the velocity vectors show that on average, water flows in at the updrift side of the gap, and flows seaward through the centre and the downwind side as rip currents (Fig. 14(a)). Horizontal flow rotation over depth, as an indicator of the three-dimensionality of the velocity profiles, is high in the area outside of the breakwater field, as a result of the presence of the return flow compensating the near-surface onshore mass flux by the incident waves, and the presence of cross-shore varying longshore currents, and of near-bed streaming. At the location of the gaps, areas of wave breaking exist, and similar flow patterns forced by wave dissipation occur there. At the tips of the breakwaters, there is strong interaction between the northward flow behind the structures, and the cross-shore flows through the gaps. In the lee of the breakwater field, the current direction is constant over depth (Fig. 14(b)).

Vertical velocity profiles vary strongly throughout the domain (Fig. 14(c)). Outside of the lee of the breakwater field (point A), we reproduce the classical vertical Eulerian velocity profile associated with wave-driven longshore flow on open beaches. Wave-driven onshore mass flux is compensated by an offshore directed return flow, and the longshore velocity profile has a logarithmic shape. Behind the most updrift breakwater (point B), the shore is more protected from the incident waves, and the cross-shore velocity is close to zero, and more depth-uniform. The longshore current at B however has the same shape and magnitude as in point A. In point C, at the location of the most downdrift gap between the breakwaters, the cross-shore velocity profile

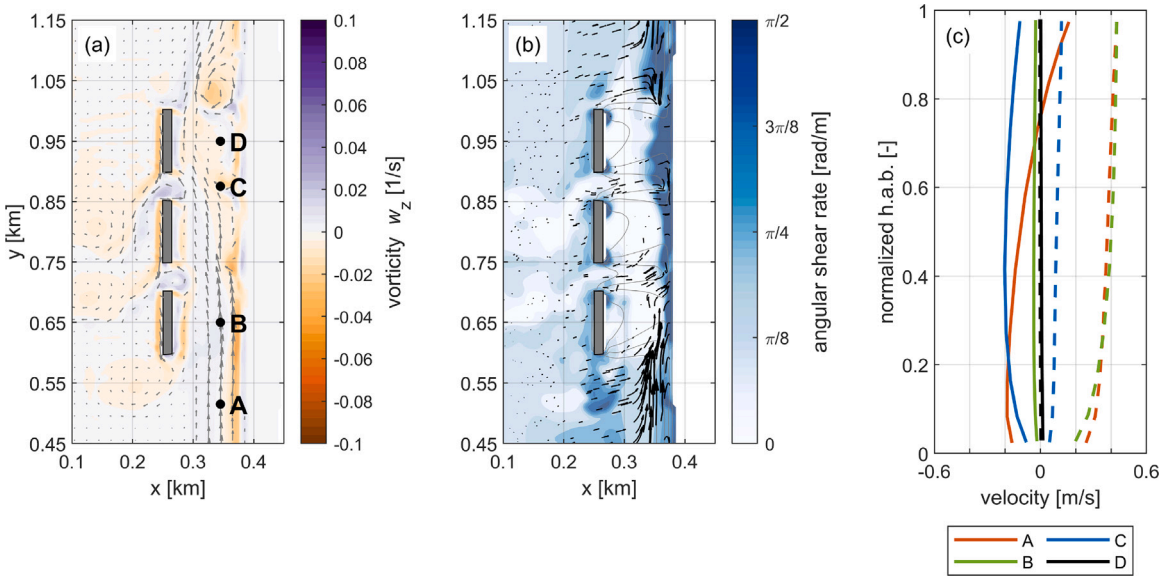

Fig. 14. Breakwater field test case. Hydrodynamics for H_s = 0.9 m, T_p = 5.2 s, θ_{inc} = 250° after 3 days of morphological change. (a) Vertical component GLM vorticity tensor w_z. Grey arrows: GLM depth-averaged velocity field. Black dots: positions of velocity profiles in (c). (b) Mean Eulerian angular shear rate $\overline{|\mathrm{d}\theta_c/\mathrm{d}z|}$. Black arrows: total sediment transport pattern. Grey contours: H_s in 0.2 m increments. (c) Vertical Eulerian velocity profiles in stations A–D. Full: cross-shore component; Dashed: longshore component. Positive values are onshore and to the north, respectively. h.a.b = height above bed.

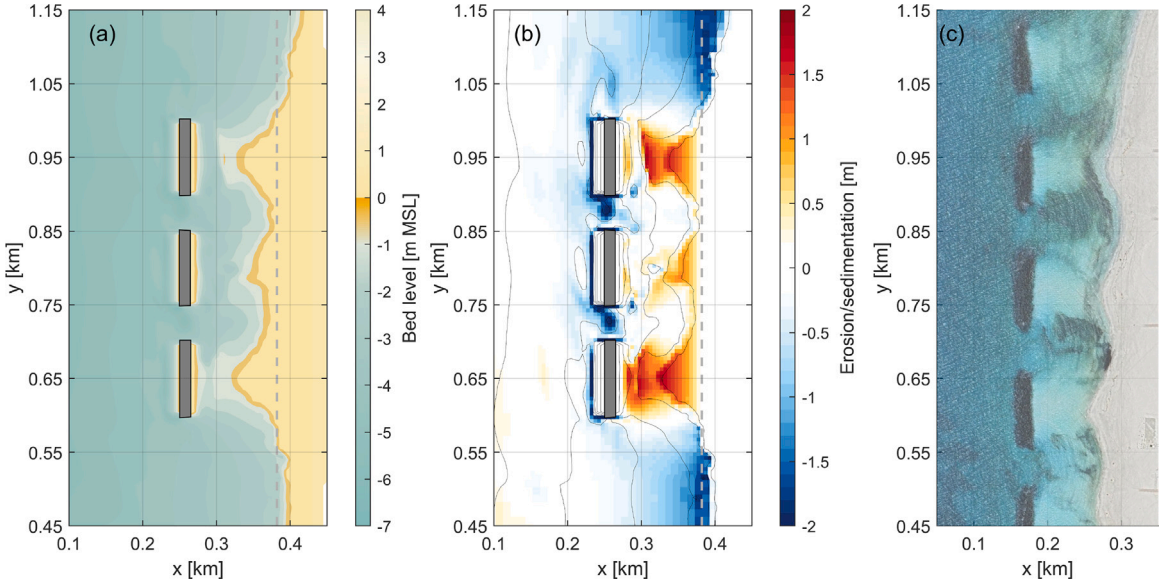

Fig. 15. Breakwater field test case. Results after 1 year of morphological change. (a) Final bathymetry; (b) Erosion/sedimentation pattern. Grey dashed line: initial coastline. (c) Breakwater field Alexandria. Satellite imagery from Google Earth.

is the result of a combination of wave-driven flow and offshore-directed flow through the gap. The longshore current magnitude is about 20 % of that of the undisturbed longshore current in point A. Finally, point D is located around the convergence point of the wave-driven longshore current, and the downwind recirculation cell, where flow is more or less stagnant for this bed level and these boundary conditions.

Based on the geometry of the system, we expect well-developed salients to build out, without shoreline erosion at the location of the gaps (Pope and Dean, 1987). After 1 year of morphological time, three salients have built out from the initial shoreline extending over a distance of 40 m to 50 m (Fig. 15(a,b)), similar to the Alexandria breakwater field that we used to dimension our model geometry and forcing conditions (Fig. 15(c)). The presence of these salients significantly reduces the longshore transport in the lee side of the breakwater field, contributing to the stability of the morphological patterns. On both updrift and downdrift sides, substantial erosion of the beach occurs, which is usually compensated by nourishments or additional structures in practice (van Rijn, 2011).

Table A.1
Defaults for main model parameters for hydrodynamics, sediment transport and morphology as used in this study.

Hydrodynamics		
Parameter	*Description*	*Value*
CFLMax	Courant-Friedrich-Lévy condition	0.7
waveturbpendepth	Penetration depth to derive wave-breaker related TKE production as fraction of H_{rms} [–]	1.5
stokesprofile	Order of the Stokes drift profile approximation [–]	2
wavestreaming	Switch to include wave streaming	Yes
rouwav	Wave–current interaction formulation according to Soulsby et al. (1993)	FR84
ftauw	Calibration parameter wave-related bed shear stress [–]	1.0
fwfac	Calibration parameter wave streaming [–]	1.0
fbreak	Calibration parameter wave-breaker related TKE production [–]	1.0
Sediment transport		
Parameter	*Description*	*Value*
Implicitfallvelocity	Settling term in vertical SSC advection eqn solved implicitly	Yes
Morphology		
Parameter	*Description*	*Value*
Thresh	Threshold sediment thickness for transport and erosion reduction [m]	0.05 h
MorUpd	Update bathymetry during simulation	Yes
DensIn	Include effect of sediment concentration on fluid density	No
AlfaBs	Streamwise bed gradient factor for bed load transport α_{bs} [–]	1.0
AlfaBn	Transverse bed gradient factor for bed load transport α_{bn} [–]	1.5
Sus	Multiplication factor for suspended sediment reference concentration κ_{sus} [–]	1.0
Bed	Multiplication factor for bed-load transport vector magnitude κ_{bed} [–]	1.0
SusW	Wave-related suspended sed. transport factor [–]	0.05
BedW	Wave-related bed-load sed. transport factor [–]	0.05
ThetSD	Factor for erosion of adjacent dry cells [–]	0.5

5. Summary and conclusions

In this study, we have presented a new 3D morphodynamic model that leverages the use of orthogonal unstructured grids for the efficient spatial discretization of the model equations, optimizing both the level of detail resolved in the model and the maximum allowed explicit time step size. The model is based on the existing 3D hydrodynamic flow solver Delft3D-FM, which was extended with formulations expressing the phase-averaged effect of short waves and surface rollers on flow momentum, turbulence and bed shear stress. The model is able to run under both stationary and non-stationary wave forcing, where the latter allows the simulation of the effect of infragravity waves on nearshore circulation, enhancing the model's capability to efficiently predict the erosion hazards associated with (extreme) storms over large domains. The model features an extensive list of sediment transport formulations that can be used in a multi-fraction model setup to simulate the morphological evolution in the domain. The addition of sediment slumping, dry cell erosion and swash zone slope relaxation in combination with a multi-layer bed stratigraphy model allows for the reproduction of morphodynamics on different time scales ranging from that of a single storm event to several years.

A number of test cases consisting of comparisons with analytical solutions, and with observations in laboratory and field settings, were undertaken to verify the robustness of the model implementation. It was shown that the model can reproduce depth-varying current profiles under breaking and non-breaking wave conditions, that it conserves sediment mass, and that after calibration, it can reproduce bedload and suspended load volumes under both tidal and wave-driven current conditions. The model results are sensitive to the vertical grid resolution, and the test cases show that in practice, 10 to 20 σ-layers are sufficient to capture the dynamics correctly, if logarithmic refinement is being used. The morphological applications in this study show the applicability of a single model framework to a wide range of common engineering challenges on open coasts, such as the assessment of beach and dune response to storms, scour prediction around breakwaters, navigation channel infilling, and inlet breaching. The comprehensive model formulations, in combination with BMI compatibility, could alleviate many of the challenges that are currently posed when trying to model longer term morphological response of coastal environments, where both storms and less energetic conditions are determining the final bed levels.

CRediT authorship contribution statement

Johan Reyns: Writing – original draft, Validation, Software, Formal analysis, Conceptualization. **Bert Jagers:** Writing – review & editing, Software. **Roshanka Ranasinghe:** Writing – review & editing, Conceptualization. **Herman Kernkamp:** Software. **Dano Roelvink:** Writing – review & editing, Software, Conceptualization.

Funding

This research was supported by Deltares, Netherlands under Strategic Research Programmes 'Natural Hazards' and 'Knowledge Foundation Software and Models', and by the Office of Naval Research, United States under award number N00014-17-1-2459.

Declaration of competing interest

The authors declare that they have no known competing financial interests or personal relationships that could have appeared to influence the work reported in this paper.

Acknowledgements

We would like to thank Mitch Harley for sharing the pre- and post-storm topographic data, and Manly Hydraulics Laboratory for providing water level data for the Narrabeen model. The support of students and many colleagues at Deltares in the testing of various iterations of the codebase is gratefully acknowledged.

Appendix A. Default model parameters

See Table A.1.

Table B.1
Error metric definitions.

Parameter	Formula (m=measured; c=computed)	Description
Coefficient of determination R^2	$\left(Cov(m,c)/\sigma_m \sigma_c\right)^2$	Indicates strength of a linear relationship between random variables m and c
Scatter Index SCI	$\frac{\sqrt{\overline{(c-m)^2}}}{\max(\sqrt{\overline{m^2}},\lvert\overline{m}\rvert)}$	Relative measure of the scatter between model and data. The error is normalized with the maximum of the rms of the data and the absolute value of the mean of the data; this avoids strange results for data with small mean and large variability
Bias	$\overline{c-m}$	Average difference between model and data
Relative bias	$\frac{\overline{c-m}}{\max(\sqrt{\overline{m^2}},\lvert\overline{m}\rvert)}$	This is a relative measure of the bias, normalized in the same way as the Scatter Index
Skill	$1.0-\frac{var(c-m)}{var(m)}$	This parameter relates the variance of the difference between data and model to the variance of the data. skill=1 means perfect skill; skill=0 means no skill; skill<0 means result is worse than doing nothing.

Table B.2
Error statistics hydrodynamic test cases. U, V: velocity components [m/s]; ZS: water level [m]; Hs: Significant wave height [m]; SSC: sediment concentration [kg/m^3]; BREACH: breach width [m]. Error metrics are defined in Table B.1.

Test case	Parameter	R^2	SCI	Rel. bias	Skill
Klopman (1994) CNW	U_{mean}	0.94	0.02	0.02	1.00
Klopman (1994) WFC	U_{mean}	0.92	0.05	0.02	1.00
Klopman (1994) WNC	U_{mean}	0.92	0.23	0.09	0.95
Klopman (1994) WOC	U_{mean}	0.95	0.05	0.02	1.00
Hamilton and Ebersole (2001) LSTF default	HS_{mean}	0.90	0.06	0.02	1.00
	ZS_{mean}	0.89	0.20	−0.03	0.96
	U_{mean}	0.73	0.41	0.28	0.80
	V_{mean}	0.40	0.14	0.08	0.98
Hamilton and Ebersole (2001) LSTF β_r −20%	HS_{mean}	0.90	0.06	0.02	1.00
	ZS_{mean}	0.89	0.20	−0.03	0.96
	U_{mean}	0.73	0.41	0.28	0.80
	V_{mean}	0.40	0.14	0.09	0.98
Hamilton and Ebersole (2001) LSTF β_r +20%	HS_{mean}	0.90	0.06	0.02	1.00
	ZS_{mean}	0.89	0.19	−0.02	0.96
	U_{mean}	0.73	0.41	0.27	0.80
	V_{mean}	0.39	0.14	0.08	0.98
Hamilton and Ebersole (2001) LSTF γ −20%	HS_{mean}	0.91	0.09	−0.08	0.99
	ZS_{mean}	0.90	0.27	−0.04	0.93
	U_{mean}	0.73	0.33	0.15	0.87
	V_{mean}	0.39	0.22	0.20	0.95
Hamilton and Ebersole (2001) LSTF γ +20%	HS_{mean}	0.88	0.12	0.09	0.99
	ZS_{mean}	0.88	0.25	0.01	0.94
	U_{mean}	0.73	0.52	0.40	0.66
	V_{mean}	0.39	0.14	0.01	0.98

Table B.3
Error statistics sediment transport/morphology test cases. U, V: velocity components [m/s]; ZS: water level [m]; Hs: Significant wave height [m]; SSC: sediment concentration [kg/m^3]; BREACH: breach width [m]. Error metrics are defined in Table B.1.

Test case	Parameter	R^2	SCI	Rel. bias	Skill
Rouse algebraic	$SSC_{10layers}$	0.87	0.12	0.02	0.99
	$SSC_{20layers}$	0.93	0.14	0.00	0.98
	$SSC_{50layers}$	0.97	0.14	−0.03	0.98
Rouse k-ϵ	$SSC_{10layers}$	0.87	0.24	0.16	0.94
	$SSC_{20layers}$	0.94	0.22	0.11	0.95
	$SSC_{50layers}$	0.97	0.19	0.06	0.96
Jacobs and Dekker (2000)	$U_{10layers}$	0.95	0.10	0.01	0.99
	$SSC_{10layers}$	0.96	0.24	−0.09	0.94
	$U_{20layers}$	0.95	0.09	0.02	0.99
	$SSC_{20layers}$	0.96	0.21	−0.08	0.95
van Rijn (1984) trench	U	0.76	0.14	−0.08	0.98
	SSC	0.89	0.28	−0.04	0.89

(continued on next page)

Table B.3 (*continued*).

Test case	Parameter	R^2	SCI	Rel. bias	Skill
	ZS	0.88	0.28	−0.01	0.89
Visser et al. (1995) Zwin breach, default	U	0.89	0.23	−0.06	0.91
	BREACH	0.91	0.14	−0.01	0.97
Visser et al. (1995) Zwin breach, −10 % transport	BREACH	0.91	0.14	−0.02	0.97
Visser et al. (1995) Zwin breach, + 10 % transport	BREACH	0.91	0.14	0.00	0.97
Visser et al. (1995) Zwin breach, dry slope 0.9	BREACH	0.91	0.14	−0.01	0.97
Visser et al. (1995) Zwin breach, VR84 transport	BREACH	0.91	0.16	0.02	0.96

Table B.4
Error statistics Narrabeen test case. ZB: bed level [m]. Error metrics are defined in Table B.1.

Test case	Parameter	Skill	Bias
ECL 2016, Base case	ZB	0.59	−0.06
ECL 2016, Wave direction −10°	ZB	0.58	−0.05
ECL 2016, Wave direction +10°	ZB	0.60	−0.07
ECL 2016, Wave height −20%	ZB	0.68	−0.07
ECL 2016, Wave height +20%	ZB	0.47	−0.06
ECL 2016, Wave period −20%	ZB	0.62	−0.07
ECL 2016, Facua −20%	ZB	0.59	−0.06
ECL 2016, Facua +20%	ZB	0.59	−0.06

Appendix B. Performance metrics verification runs

See Table B.1.
See Table B.2.
See Table B.3.
See Table B.4.

Data availability

Data will be made available on request.

References

Abreu, T., Silva, P.A., Sancho, F., Temperville, A., 2010. Analytical approximate wave form for asymmetric waves. Coast. Eng. 57 (7), 656–667.

Afzal, A., Ansari, Z., Faizabadi, A.R., Ramis, M.K., 2016. Parallelization Strategies for Computational Fluid Dynamics Software: State of the Art Review. Arch. Comput. Methods Eng. 24 (2), 337–363.

Ahrens, J.P., 2000. A fall-velocity equation. J. Waterw. Port Coast. Ocean. Eng. 126 (2), 99–102.

Albernaz, M. Boechat, Ruessink, G., Jagers, H.R.A.B., Kleinhans, M.G., 2019. Effects of Wave Orbital Velocity Parameterization on Nearshore Sediment Transport and Decadal Morphodynamics. J. Mar. Sci. Eng. 7 (6), 188.

Andrews, D.G., McIntyre, M.E., 1978. An exact theory of nonlinear waves on a Lagrangian-mean flow. J. Fluid Mech. 89 (4), 609–646.

Ardhuin, F., Jenkins, A.D., 2006. On the interaction of surface waves and upper ocean turbulence. J. Phys. Oceanogr. 36 (3), 551–557.

Bagnold, R.A., 1966. An approach to the sediment transport problem from general physics. Geol. Surv. Prof. Pap. 42, 37.

Baldock, T., Holmes, P., Bunker, S., Van Weert, P., 1998. Cross-shore hydrodynamics within an unsaturated surf zone. Coast. Eng. 34 (3–4), 173–196.

Beuzen, T., Harley, M.D., Splinter, K.D., Turner, I.L., 2019. Controls of variability in berm and dune storm erosion. J. Geophys. Res.: Earth Surf. 124 (11), 2647–2665.

Bokuniewicz, H.J., Kraus, N.C., Munger, S., Slattery, M., Coffey, R., 2011. Monitoring incipient breaching at an artificial inlet: Georgica pond, new york. J. Coast. Res. 59, 111–117.

Booij, N., Ris, R.C., Holthuijsen, L.H., 1999. A third-generation wave model for coastal regions: 1. model description and validation. J. Geophys. Res.: Ocean. 104 (C4), 7649–7666.

Bracs, M., 2016. Efficient Monitoring of Sandy Shoreline Variability At the Regional Scale (Ph.D. thesis). School of Civil and Environmental Engineering, Faculty of Engineering, UNSW.

Bryant, D.B., Bryant, M.A., Grzegorzewski, A.S., 2017. Erosion of Coastal Foredunes: A Review on the Effect of Dune Vegetation. Tech Report ERDC/CHL CHETN-I-94, USACE.

Chassagne, C., Safar, Z., 2020. Modelling flocculation: Towards an integration in large-scale sediment transport models. Mar. Geol. 430, 106361.

Chassignet, E.P., Hurlburt, H.E., Smedstad, O.M., Halliwell, G.R., Hogan, P.J., Wallcraft, A.J., Baraille, R., Bleck, R., 2007. The HYCOM (hybrid coordinate ocean model) data assimilative system. J. Mar. Syst. 65 (1–4), 60–83.

Chen, C., Beardsley, R., Cowles, G., 2006. An Unstructured Grid, Finite-Volume Coastal Ocean Model (FVCOM) System. Oceanography 19 (1), 78–89.

Colebrook, C.F., White, C.M., 1937. Experiments with fluid friction in roughened pipes. Proc. R. Soc. Lond. Ser. A-Mathematical Phys. Sci. 161 (906), 367–381.

Cuddington, K., Fortin, M.-J., Gerber, L.R., Hastings, A., Liebhold, A., O'Connor, M., Ray, C., 2013. Process-based models are required to manage ecological systems in a changing world. Ecosphere 4 (2), 1–12.

De Vet, L.M., McCall, R.T., Den Bieman, J.P., Stive, M.J.F., Van Ormondt, M., 2015. Modelling dune erosion, overwash and breaching at fire island (NY) during hurricane sandy. In: Coastal Sediments 2015. World Scientific.

Dean, R.G., Dalrymple, R.A., 1991. Water Wave Mechanics for Engineers and Scientists. World Scientific Publishing Co Pte Ltd.

Deltares, 2025a. D-Flow Flexible Mesh, Technical Reference Manual. Technical Report.

Deltares, 2025b. D-Morphology, 1D/2D/3D, User Manual. Technical Report.

Dethier, E.N., Renshaw, C.E., Magilligan, F.J., 2022. Rapid changes to global river suspended sediment flux by humans. Science 376 (6600), 1447–1452.

Dey, S., 2003. Threshold of sediment motion on combined transverse and longitudinal sloping beds. J. Hydraul. Res. 41 (4), 405–415.

Dingemans, M.W., Radder, A.C., De Vriend, H.J., 1987. Computation of the driving forces of wave-induced currents. Coast. Eng. 11 (5–6), 539–563.

Dodman, D., Hayward, B., Pelling, M., Broto, V.Castan., Chow, W., Chu, E., Dawson, R., Khirfan, L., McPhearson, T., Prakash, A., Zheng, Y., Ziervogel, G., 2022. Cities, settlements and key infrastructure. In: Pörtner, H.O., Roberts, D.C., Tignor, M., Poloczanska, E.S., Mintenbeck, K., Alegrí a, A., Craig, M., Langsdorf, S., Löschke, S., Möller, V., Okem, A., Rama, B. (Eds.), Climate Change 2022: Impacts, Adaptation and Vulnerability. Contribution of Working Group II To the Sixth Assessment Report of the Intergovernmental Panel on Climate Change, Book Section 6. Cambridge University Press, Cambridge, UK and New York, NY, USA.

Durrant, T., Hemer, M., Smith, G., Trenham, C., Greenslade, D., 2019. CAWCR Wave Hindcast - Aggregated Collection. V5. Technical Report, CSIRO.

Egbert, G.D., Erofeeva, S.Y., 2002. Efficient inverse modeling of barotropic ocean tides. J. Atmos. Ocean. Technol. 19 (2), 183–204.

Feddersen, F., 2012. Scaling surf zone turbulence. Geophys. Res. Lett. 39 (18).

Feddersen, F., Trowbridge, J.H., 2005. The effect of wave breaking on surf-zone turbulence and alongshore currents: A modeling study*. J. Phys. Oceanogr. 35 (11), 2187–2203.

Fox-Kemper, B., Hewitt, H.T., Xiao, C., Aðalgeirsdóttir, G., Drijfhout, S.S., Edwards, T.L., Golledge, N.R., Hemer, M., Kopp, R.E., Krinner, G., Mix, A., Notz, D., Nowicki, S., Nurhati, I.S., Ruiz, L., Sallée, J.-B., Slangen, A.B.A., Yu, Y., 2021. Ocean, cryosphere and sea level change. In: Masson-Delmotte, V., Zhai, P., Pirani, A., Connors, S.L., Péan, C., Berger, S., Caud, N., Chen, Y., Goldfarb, L., Gomis, M.I., Huang, M., Leitzell, K., Lonnoy, E., Matthews, J.B.R., Maycock, T.K., Waterfield, T., Yelek¸ci, O., Yu, R., Zhou, B. (Eds.), Climate Change 2021: The Physical Science Basis. Contribution of Working Group I To the Sixth Assessment Report of the Intergovernmental Panel on Climate Change, Book Section 9. Cambridge University Press, Cambridge, UK and New York, NY, USA, pp. 1211–1361.

Fredsøe, J., Deigaard, R., 1992. Mechanics of Coastal Sediment Transport. World Scientific Publishing Co Pte Ltd.

Galappatti, G., Vreugdenhil, C.B., 1985. A depth-integrated model for suspended sediment transport. J. Hydraul. Res. 23 (4), 359–377.

Garcez Faria, A.F., Thornton, E.B., Stanton, T.P., Soares, C.V., Lippmann, T.C., 1998. Vertical profiles of longshore currents and related bed shear stress and bottom roughness. J. Geophys. Res.: Ocean. 103 (C2), 3217–3232.

Google, 2022. Google earth.

Guth, P.L., Trevisani, S., Grohmann, C.H., Lindsay, J., Gesch, D., Hawker, L., Bielski, C., 2024. Ranking of 10 global one-arc-second dems reveals limitations in terrain morphology representation. Remote. Sens. 16 (17), 3273.
Hamilton, D.G., Ebersole, B.A., 2001. Establishing uniform longshore currents in a large-scale sediment transport facility. Coast. Eng. 42 (3), 199–218.
Harley, M.D., Turner, I.L., Kinsela, M.A., Middleton, J.H., Mumford, P.J., Splinter, K.D., Phillips, M.S., Simmons, J.A., Hanslow, D.J., Short, A.D., 2017. Extreme coastal erosion enhanced by anomalous extratropical storm wave direction. Sci. Rep. 7 (1).
Hendy, D.M., El-Geziry, T.M., El Raey, M., Nasr, S.M., 2021. Sea level characteristics and extremes along Alexandria coastal zone. Arab. J. Geosci. 14 (13).
Hersbach, H., Bell, B., Berrisford, P., Hirahara, S., Horányi, A., Muñoz-Sabater, J., Nicolas, J., Peubey, C., Radu, R., Schepers, D., Simmons, A., Soci, C., Abdalla, S., Abellan, X., Balsamo, G., Bechtold, P., Biavati, G., Bidlot, J., Bonavita, M., De Chiara, G., Dahlgren, P., Dee, D., Diamantakis, M., Dragani, R., Flemming, J., Forbes, R., Fuentes, M., Geer, A., Haimberger, L., Healy, S., Hogan, R.J., Hólm, E., Janisková, M., Keeley, S., Laloyaux, P., Lopez, P., Lupu, C., Radnoti, G., de Rosnay, P., Rozum, I., Vamborg, F., Villaume, S., Thépaut, J., 2020. The era5 global reanalysis. Q. J. R. Meteorol. Soc. 146 (730), 1999–2049.
Hirano, M., 1971. River-bed degradation with armoring. In: Proceedings of the Japan Society of Civil Engineers, vol. 1971, Japan Society of Civil Engineers, pp. 55–65.
Hjelmfelt, A.T., Lenau, C.W., 1970. Nonequilibrium transport of suspended sediment. J. Hydraul. Div. 96 (7), 1567–1586.
Holthuijsen, L., Herman, A., Booij, N., 2003. Phase-decoupled refraction–diffraction for spectral wave models. Coast. Eng. 49 (4), 291–305.
Hsu, J.R.C., Silvester, R., 1990. Accretion behind single offshore breakwater. J. Waterw. Port Coast. Ocean. Eng. 116 (3), 362–380.
Hunt, E., Davidson, M., Steele, E.C.C., Amies, J.D., Scott, T., Russell, P., 2023. Shoreline modelling on timescales of days to decades. Camb. Prism.: Coast. Futur. 1.
Hutton, E.W., Piper, M.D., Tucker, G.E., 2020. The basic model interface 2.0: A standard interface for coupling numerical models in the geosciences. J. Open Source Softw. 5 (51), 2317.
Ikeda, S., 1982. Incipient Motion of Sand Particles on Side Slopes. J. Hydraul. Div. 108 (1), 95–114.
Iskander, M.M., Frihy, O.E., El Ansary, A.E., Abd El Mooty, M.M., Nagy, H.M., 2007. Beach impacts of shore-parallel breakwaters backing offshore submerged ridges, Western Mediterranean Coast of Egypt. J. Environ. Manag. 85 (4), 1109–1119.
Isobe, M., Horikawa, K., 1982. Study on Water Particle Velocities of Shoaling and Breaking Waves. Coast. Eng. Jpn. 25 (1), 109–123.
Jacobs, C., Dekker, S., 2000. Sediment concentrations due to currents and irregular waves. In: The Effects of Grading of the Bed Material. Measurements Report. Technical Report, Delft University of Technology.
Jones, W., Launder, B., 1972. The prediction of laminarization with a two-equation model of turbulence. Int. J. Heat Mass Transfer 15 (2), 301–314.
Justesen, P., Fredsøe, J., Deigaard, R., 1987. The bottleneck problem for turbulence in relation to suspended sediment in the surf zone. In: Coastal Engineering 1986. American Society of Civil Engineers, pp. 1225–1239.
Kernkamp, H.W.J., Van Dam, A., Stelling, G.S., de Goede, E.D., 2011. Efficient scheme for the shallow water equations on unstructured grids with application to the continental shelf. Ocean. Dyn. 61 (8), 1175–1188.
Kleptsova, O., Pietrzak, J., Stelling, G., 2009. On the accurate and stable reconstruction of tangential velocities in c-grid ocean models. Ocean. Model. 28 (1–3), 118–126.
Klopman, G., 1994. Vertical structure of the flow due to waves and currents. In: Laser–Doppler Flow Measurements for Waves Following Or Opposing a Current. Technical Report, WL|Delft Hydraulics.
Krone, R., 1962. Flume studies of the transport of sediment in estuarial shoaling processes final report.
Latteux, B., 1995. Techniques for long-term morphological simulation under tidal action. Mar. Geol. 126 (1–4), 129–141.
Launder, B., Spalding, D.B., 1972. Mathematical Models of Turbulence. Academic Press, San Diego, CA.
Le, N.A., 2012. Validation of 3D Wave-Driven Flow Modeling in Delft3D. (Master's thesis). UNESCO-IHE.
van Ledden, M., 2002. A process-based sand-mud model. In: Winterwerp, J.C., Kranenburg, C. (Eds.), Fine Sediment Dynamics in the Marine Environment. Elsevier, pp. 577–594.
Lesser, G.R., 2009. An Approach To Medium-Term Coastal Morphological Modelling (Ph.D. thesis). IHE Delft & Delft University of Technology.
Lesser, G., Roelvink, J., van Kester, J., Stelling, G., 2004. Development and validation of a three-dimensional morphological model. Coast. Eng. vol. 51 (8–9), 883–915.
Lobeto, H., Menendez, M., Losada, I.J., Hemer, M., 2022. The effect of climate change on wind-wave directional spectra. Glob. Planet. Change 213, 103820.
Longuet-Higgins, M.S., 1953. Mass transport in water waves. Philos. Trans. R. Soc. Lond. Ser. A Math. Phys. Sci. 245 (903), 535–581.
López-Ramade, E., Mulligan, R.P., Medellín, G., Torres-Freyermuth, A., 2023. Modelling beach morphological responses near coastal structures under oblique waves driven by sea-breezes. Coast. Eng. 182, 104290.
van der Lugt, M.A., Quataert, E., van Dongeren, A., van Ormondt, M., Sherwood, C.R., 2019. Morphodynamic modeling of the response of two barrier islands to atlantic hurricane forcing. Estuar. Coast. Shelf Sci. 229, 106404.
Lyn, D.A., Altinakar, M., 2002. St. Venant–Exner equations for near-critical and transcritical flows.. J. Hydraul. Eng. vol. 128 (6), 579–587.
Manning, A., Dyer, K., 2007. Mass settling flux of fine sediments in northern European estuaries: Measurements and predictions. Mar. Geol. 245 (1–4), 107–122.
Martyr-Koller, R., Kernkamp, H., van Dam, A., van der Wegen, M., Lucas, L., Knowles, N., Jaffe, B., Fregoso, T., 2017. Application of an unstructured 3d finite volume numerical model to flows and salinity dynamics in the san francisco bay-delta. Estuar. Coast. Shelf Sci. 192, 86–107.
McFall, B.C., 2019. The Relationship between Beach Grain Size and Intertidal Beach Face Slope. J. Coast. Res. 35 (5), 1080.
Meyer-Peter, E., Müller, R., 1948. Formulas for bed-load transport. In: Second Meeting IAHR.
MHL, 2022a. Water Level Data Fort Benison Tide Gauge. Technical Report, Manly Hydraulics Laboratory, Manly Vale, NSW.
MHL, 2022b. Water Level Data Ocean Street Bridge Gauge, Narrabeen. Technical Report, Manly Hydraulics Laboratory, Manly Vale, NSW.
Moghimi, S., Thomson, J., Özkan Haller, T., Umlauf, L., Zippel, S., 2016. On the modeling of wave-enhanced turbulence nearshore. Ocean. Model. 103, 118–132.
Morris, P.H., Williams, D.J., 1996. Relative celerities of mobile bed flows with finite solids concentrations. J. Hydraul. Eng. 122 (6), 311–315.
Mortlock, T., Goodwin, I., McAneney, J., Roche, K., 2017. The 2016 Australian East Coast low: Importance of wave direction for coastal erosion assessment. Water 9 (2), 121.
Mory, M., Hamm, L., 1997. Wave height, setup and currents around a detached breakwater submitted to regular or random wave forcing. Coast. Eng. 31 (1–4), 77–96.
Nairn, R.B., Roelvink, J.A., Southgate, H.N., 1990. Transition zone width and implications for modelling surfzone hydrodynamics. In: Coastal Engineering 1990. pp. 68–81.
Nawarat, K., Reyns, J., Vousdoukas, M.I., Duong, T.M., Kras, E., Ranasinghe, R., 2024. Coastal hardening and what it means for the world's sandy beaches. Nat. Commun. 15 (1).
Nguyen, D.T., Jacobsen, N.G., Roelvink, D., 2021. Development and Validation of Quasi-Eulerian Mean Three-Dimensional Equations of Motion Using the Generalized Lagrangian Mean Method. J. Mar. Sci. Eng. 9 (1), 76.
Nielsen, P., 1992. Coastal Bottom Boundary Layers and Sediment Transport. World Scientific Publishing Co Pte Ltd.
Nienhuis, J.H., van de Wal, R.S.W., 2021. Projections of Global Delta Land Loss From Sea-Level Rise in the 21st Century. Geophys. Res. Lett. 48 (14).
NSW DCCEEW, 2019. NSW Marine LiDAR Topo-Bathy 2018. Technical Report, NSW Department of Climate Change, Energy, the Environment and Water.
NSW DCCEEW, 2022. NSW Seabed Landforms Derived from Marine Lidar Data 2022. Technical Report, NSW Department of Climate Change, Energy, the Environment and Water.
Nsw DPI, 2019. NSW Marine LiDAR Topo-Bathy 2018 Geotif. Technical Report, NSW Department of Planning, Industry and Environment.
Olabarrieta, M., Warner, J.C., Hegermiller, C.A., 2023. Development and Application of an Infragravity Wave (InWave) Driver to Simulate Nearshore Processes. J. Adv. Model. Earth Syst. 15 (6).
Open Street Mapc ontributors, 2022. Planet dump. retrieved from https://www.openstreetmap.org. (Accessed 24 June 2022).
Palmsten, M.L., Holman, R.A., 2012. Laboratory investigation of dune erosion using stereo video. Coast. Eng. 60, 123–135.
Partheniades, E., 1965. Erosion and deposition of cohesive soils. J. Hydraul. Div. 91 (1), 105–139.
Perot, B., 2000. Conservation properties of unstructured staggered mesh schemes. J. Comput. Phys. 159 (1), 58–89.
Pope, J., Dean, J.L., 1987. Development of design criteria for segmented breakwaters. In: Coastal Engineering 1986. Proceedings 20th International Conference on Coastal Engineering. ASCE, Taipei, Taiwan, pp. 2144–2158.
Prandtl, L., 1905. Űber flüssigkeitsbewegung bei sehr kleiner reibung.
Priestley, M.D.K., Catto, J.L., 2022. Future changes in the extratropical storm tracks and cyclone intensity, wind speed, and structure. Weather. Clim. Dyn. 3 (1), 337–360.
Reeve, D., Chadwick, A., Fleming, C., 2018. Coastal Engineering: Processes, Theory and Design Practice. CRC Press.
Reeve, D.E., Karunarathna, H., Pan, S., Horrillo-Caraballo, J.M., Różyński, G., Ranasinghe, R., 2016. Data-driven and hybrid coastal morphological prediction methods for mesoscale forecasting. Geomorphology 256, 49–67.
Reis, A.H., Gama, C., 2010. Sand size versus beachface slope — an explanation based on the constructal law. Geomorphology 114 (3), 276–283.
Reyns, J., McCall, R., Ranasinghe, R., van Dongeren, A., Roelvink, D., 2023. Modelling wave group-scale hydrodynamics on orthogonal unstructured meshes. Environ. Model. Softw. 162, 105655.
Richardson, J., Zaki, W., 1954. Sedimentation and fluidisation: Part i. Trans. Inst. Chem. Eng. 32, 35–53.
van Rijn, L.C., 1980. Computation of Siltation in Dredged Trenches. Technical Report 1267-V, WL| Delft Hydraulics, Delft, the Netherlands.
van Rijn, L.C., 1984. Sediment transport, part II: suspended load transport. J. Hydraul. Eng. 110 (11), 1613–1641.

van Rijn, L.C., 1993. Principles of Sediment Transport in Rivers, Estuaries and Coastal Seas. Aqua Publications, the Netherlands.
van Rijn, L.C., 2006. Principles of Sediment Transport in Rivers, Estuaries and Coastal Seas, Part 2. Aqua Publications, the Netherlands.
van Rijn, L.C., 2007a. Unified View of Sediment Transport by Currents and Waves. I: Initiation of Motion, Bed Roughness, and Bed-Load Transport. J. Hydraul. Eng. 133 (6), 649–667.
van Rijn, L.C., 2007b. Unified View of Sediment Transport by Currents and Waves. II: Suspended Transport. J. Hydraul. Eng. 133 (6), 668–689.
van Rijn, L.C., 2007c. Unified View of Sediment Transport by Currents and Waves. III: Graded Beds. J. Hydraul. Eng. 133 (7), 761–775.
van Rijn, L.C., 2011. Coastal erosion and control. Ocean & Coastal Management 54 (12), 867–887.
Rodi, W., 1987. Examples of calculation methods for flow and mixing in stratified fluids. J. Geophys. Res.: Ocean. 92 (C5), 5305–5328.
Rodi, W., 1993. Turbulence Models and their Application in Hydraulics, third ed. Balkema, Rotterdam.
Roelvink, J.A., 2006. Coastal morphodynamic evolution techniques. Coast. Eng. 53 (2–3), 277–287.
Roelvink, D., Costas Otero, S., 2017. Beach berms as an essential link between subaqueous and subaerial beach/dune profiles. Geotemas (17), 79–82.
Roelvink, D., Mccall, R., Costas, S., van der Lugt, M., 2019. Controlling swash zone slope is key to beach profile modelling. In: Coastal Sediments 2019: Proceedings of the 9th International Conference. World Scientific, pp. 149–157.
Roelvink, D., Reniers, A., van Dongeren, A., van Thiel de Vries, J., McCall, R., Lescinski, J., 2009. Modelling storm impacts on beaches, dunes and barrier islands. Coast. Eng. 56 (11–12), 1133–1152.
Rosati, J.D., Gravens, M.B., Chasten, M.A., 1992. Development of detached breakwater design criteria using a shoreline response model. In: Coastal Engineering Practice. ASCE, pp. 814–829.
Ruessink, B.G., Miles, J.R., Feddersen, F., Guza, R.T., Elgar, S., 2001. Modeling the alongshore current on barred beaches. J. Geophys. Res.: Ocean. 106 (C10), 22451–22463.
Ruessink, B., Ramaekers, G., van Rijn, L., 2012. On the parameterization of the free-stream non-linear wave orbital motion in nearshore morphodynamic models. Coast. Eng. 65, 56–63.
Sallenger, A.H.J., 2000. Storm impact scale for barrier islands. J. Coast. Res. 16 (3), 890–895.
Sanders, B.F., 2008. Integration of a shallow water model with a local time step. J. Hydraul. Res. 46 (4), 466–475.
Sherwood, C.R., van Dongeren, A., Doyle, J., Hegermiller, C.A., Hsu, T.-J., Kalra, T.S., Olabarrieta, M., Penko, A.M., Rafati, Y., Roelvink, D., van der Lugt, M., Veeramony, J., Warner, J.C., 2022. Modeling the morphodynamics of coastal responses to extreme events: What shape are we in?. Annu. Rev. Mar. Sci. 14 (1), 457–492.
Smagorinsky, J., 1963. General Circulation Experiments With The Primitive Equations: I. The Basic Experiment. Mon. Weather Rev. 91 (3), 99–164.
Soulsby, R., 1997. Dynamics of Marine Sands. Thomas Telford Publishing.
Soulsby, R.L., Clarke, S., 2005. Bed Shear-Stress under Combined Waves and Currents on Smooth and Rough Beds. Technical Report 137, HR Wallingford, Wallingford.
Soulsby, R., Hamm, L., Klopman, G., Myrhaug, D., Simons, R., Thomas, G., 1993. Wave–current interaction within and outside the bottom boundary layer. Coast. Eng. 21 (1–3), 41–69.
Stive, M.J.F., Wind, H.G., 1986. Cross-shore mean flow in the surf zone. Coast. Eng. 10 (4), 325–340.
Svendsen, I., 1984. Wave heights and set-up in a surf zone. Coast. Eng. 8 (4), 303–329.
Tambroni, N., Blondeaux, P., Vittori, G., 2015. A simple model of wave–current interaction. J. Fluid Mech. 775, 328–348.
van Thiel de Vries, J.S.M., Van Gent, M.R.A., Walstra, D.J.R., Reniers, A.J.H.M., 2008. Analysis of dune erosion processes in large-scale flume experiments. Coast. Eng. 55 (12), 1028–1040.
Turner, I.L., Harley, M.D., Short, A.D., Simmons, J.A., Bracs, M.A., Phillips, M.S., Splinter, K.D., 2016. A multi-decade dataset of monthly beach profile surveys and inshore wave forcing at narrabeen, Australia. Sci. Data 3 (1).
Van Kessel, T., Winterwerp, H., Van Prooijen, B., Van Ledden, M., Borst, W., 2011. Modelling the seasonal dynamics of SPM with a simple algorithm for the buffering of fines in a sandy seabed. Cont. Shelf Res. 31 (10), S124–S134.
Villaret, C., Hervouet, J.-M., Kopmann, R., Merkel, U., Davies, A.G., 2013. Morphodynamic modeling using the Telemac finite-element system. Comput. Geosci. 53, 105–113.
Visser, P.J., 1995. A model for breach growth in Sand-Dikes. In: 24th International Conference on Coastal Engineering. American Society of Civil Engineers. American Society of Civil Engineers.
Visser, P.J., 1999. Breach erosion in sand-dikes. In: Coastal Engineering 1998. Proceedings 26th International Conference on Coastal Engineering. Copenhagen, Denmark, pp. 3516–3528.
Visser, P.J., Kraak, A.W., Bakker, W.T., Smit, M.J., Snip, D.W., Steetzel, H.J., van de Graaff, J., 1995. A large-scale experiment on breaching in sand-dikes. In: Coastal Dynamics 1995–Proceedings of the International Conference on Coastal Research in Terms of Large Scale Experiments. pp. 583–594.
Visser, P., Smit, M., Snip, D., 1996. Zwin '94 Experiment: Meetopstelling En Overzicht Van Alle Meetresultaten. Technical Report 4-96, Hydraulic Engineering Department, Delft University of Technology.
van Thiel de Vries, J.S.M., 2009. Dune Erosion During Storm Surges (Ph.D dissertation). Delft University of Technology.
Walstra, D.J.R., Hoekstra, R., Tonnon, P.K., Ruessink, B.G., 2013. Input reduction for long-term morphodynamic simulations in wave-dominated coastal settings. Coast. Eng. 77, 57–70.
Walstra, D.J.R., van Rijn, L.C., van Ormondt, M., Briere, C., Talmon, A.M., 2007. The effects of bed slope and wave skewness on sediment transport and morphology. In: Kraus, N., Dean Rosati, J. (Eds.), Proceedings of the Sixth International Symposium on Coastal Engineering and Science of Coastal Sediment Processes. American Society of Civil Engineers ASCE, United States, pp. 1–14, Coastal Sediments 2007 ; Conference date 13-05-2007 Through 17-05-2007.
Walstra, D.J.R., Roelvink, J.A., Groeneweg, J., 2001. Calculation of wave-driven currents in a 3d mean flow model. In: Coastal Engineering 2000. American Society of Civil Engineers, pp. 1050–1063.
Warner, J.C., Armstrong, B., He, R., Zambon, J.B., 2010. Development of a Coupled Ocean–Atmosphere–Wave–Sediment Transport (COAWST) Modeling System. Ocean. Model. 35 (3), 230–244.
Weatherall, P., Marks, K.M., Jakobsson, M., Schmitt, T., Tani, S., Arndt, J.E., Rovere, M., Chayes, D., Ferrini, V., Wigley, R., 2015. A new digital bathymetric model of the world's oceans. Earth Space Sci. 2 (8), 331–345.
Wiegel, R.L., 2005. Oceanographical engineering. In: Dover Books on Engineering. Dover Publications, Mineola, NY, Literaturangaben.
Wu, W., Wan, L., 2024. Coastal Ecological and Environmental Management under Multiple Anthropogenic Pressures. Elsevier, pp. 385–415.
Xu, P., Tsendbazar, N.-E., Herold, M., de Bruin, S., Koopmans, M., Birch, T., Carter, S., Fritz, S., Lesiv, M., Mazur, E., Pickens, A., Potapov, P., Stolle, F., Tyukavina, A., Van De Kerchove, R., Zanaga, D., 2024. Comparative validation of recent 10 m-resolution global land cover maps. Remote Sens. Environ. 311, 114316.
Zijlema, M., 2010. Computation of wind-wave spectra in coastal waters with SWAN on unstructured grids. Coast. Eng. 57 (3), 267–277.
Zyserman, J.A., Johnson, H.K., 2002. Modelling morphological processes in the vicinity of shore-parallel breakwaters. Coast. Eng. 45 (3–4), 261–284.